bioRxiv preprint doi: https://doi.org/10.1101/389080; this version posted November 4, 2019. The copyright holder for this preprint (which was not certified by peer review) is the author/funder, who has granted bioRxiv a license to display the preprint in perpetuity. It is made available under aCC-BY 4.0 International license.

PCH-2^{TRIP13} regulates spindle checkpoint strength

Lénaïg Défachelles, Anna E. Russo, Christian R. Nelson and Needhi Bhalla*

Department of Molecular, Cell and Developmental Biology, University of California,

Santa Cruz,

Santa Cruz, CA 95064

*corresponding author: nbhalla@ucsc.edu

Department of Molecular, Cell and Developmental Biology

225 Sinsheimer Labs

University of California, Santa Cruz

Santa Cruz, CA 95064

phone: (831) 459-1319

fax: (831) 459-3139

Key words: *C. elegans*, mitosis, embryo, spindle assembly checkpoint, Mad2,

aneuploidy, germline

bioRxiv preprint doi: https://doi.org/10.1101/389080; this version posted November 4, 2019. The copyright holder for this preprint (which was not certified by peer review) is the author/funder, who has granted bioRxiv a license to display the preprint in perpetuity. It is made available under aCC-BY 4.0 International license.

ABSTRACT

Spindle checkpoint strength is dictated by the number of unattached kinetochores, cell volume and cell fate. We show that the conserved AAA-ATPase, PCH-2/TRIP13, which remodels the checkpoint effector Mad2 from an active conformation to an inactive one, controls checkpoint strength in *C. elegans*. When we manipulate embryos to decrease cell volume, PCH-2 is no longer required for the spindle checkpoint or recruitment of Mad2 at unattached kinetochores. This role is not limited to large cells: the stronger checkpoint in germline precursor cells also depends on PCH-2. PCH-2 is enriched in germline precursor cells and this enrichment relies on a conserved factor that induces asymmetry in the early embryo. Finally, the stronger checkpoint in germline precursor cells is regulated by CMT-1, the ortholog of p31comet, which is required for both PCH-2's localization to unattached kinetochores and its enrichment in germline precursor cells. Thus, PCH-2, likely by regulating the availability of inactive Mad2 at and near unattached kinetochores, governs checkpoint strength.

bioRxiv preprint doi: https://doi.org/10.1101/389080; this version posted November 4, 2019. The copyright holder for this preprint (which was not certified by peer review) is the author/funder, who has granted bioRxiv a license to display the preprint in perpetuity. It is made available under aCC-BY 4.0 International license.

INTRODUCTION

To prevent the missegregation of chromosomes and the production of daughter cells with an incorrect number of chromosomes, the spindle checkpoint (also called the spindle assembly checkpoint) monitors whether chromosomes are attached to the spindle via kinetochores. If kinetochores fail to attach properly, this checkpoint delays the cell cycle to promote error correction and prevent aneuploidy. Despite its critical role, the duration of the cell cycle delay, defined as the strength of the spindle checkpoint, can be highly variable. This variability can be controlled by the number of unattached kinetochores (Collin et al., 2013), cell volume (Galli and Morgan, 2016; Kyogoku and Kitajima, 2017), and cell fate (Galli and Morgan, 2016; Gerhold et al., 2018).

The spindle checkpoint response initiates with the recruitment of Mad1 and Mad2 at unattached kinetochores (Chen et al., 1998; Chen et al., 1996; Li and Benezra, 1996; Sironi et al., 2001), which catalyzes the production of a Mitotic Checkpoint Complex (MCC). The MCC enforces a checkpoint arrest by inhibiting the Anaphase Promoting Complex/Cyclosome (APC/C) and preventing cell cycle progression (Sudakin et al., 2001). Formation of the MCC is driven by conformational changes in Mad2, which can exist in an open conformation (O-Mad2) or a closed conformation (C-Mad2) (Luo et al., 2002; Luo et al., 2004; Sironi et al., 2002). Mad2 is in the closed conformation in the Mad1/Mad2 tetramer recruited to unattached kinetochores. C-Mad2 in the tetramer acts as a template to convert additional soluble O-Mad2 to C-Mad2, which can be assembled into the MCC (De Antoni et al., 2005; Fava et al., 2011; Simonetta et al., 2009; Sironi et al., 2001). Thus, unattached kinetochores act as a platform for MCC assembly. The MCC effectively tunes the spindle checkpoint response: the length of the cell cycle delay imposed by the checkpoint is governed by the ratio of the soluble MCC checkpoint signal

bioRxiv preprint doi: https://doi.org/10.1101/389080; this version posted November 4, 2019. The copyright holder for this preprint (which was not certified by peer review) is the author/funder, who has granted bioRxiv a license to display the preprint in perpetuity. It is made available under aCC-BY 4.0 International license.

to cytoplasmic volume (Collin et al., 2013; Dick and Gerlich, 2013; Galli and Morgan, 2016; Kyogoku and Kitajima, 2017).

PCH-2/TRIP13 is a hexameric AAA+ ATPase that remodels HORMA domain-containing proteins, a group that includes Mad2 (Aravind and Koonin, 1998; Rosenberg and Corbett, 2015; Vader, 2015). Biochemical and structural studies have shown that PCH-2 converts C-Mad2 to O-Mad2 (Alfieri et al., 2018; Brulotte et al., 2017; Ye et al., 2015). Originally described as a spindle checkpoint silencing protein, experiments showed that TRIP13 works with the adaptor protein p31^{comet} to extract C-Mad2 from the MCC and promote its disassembly, permitting the activation of the APC/C (Alfieri et al., 2018; Brulotte et al., 2017; Eytan et al., 2014; Miniowitz-Shemtov et al., 2015; Wang et al., 2014; Ye et al., 2015). In addition, we and others have shown that PCH-2/TRIP13 is essential for spindle checkpoint activation in *C. elegans* and mammalian cells (Ma and Poon, 2016; Ma and Poon, 2018; Nelson et al., 2015; Yost et al., 2017). PCH-2 is present at unattached kinetochores (Nelson et al., 2015; Tipton et al., 2012; Wang et al., 2014) and is required to robustly localize Mad2, but not Mad1, to unattached kinetochores (Nelson et al., 2015; Yost et al., 2017).

Altogether, these data suggest that there is a significant population of C-Mad2 in cells that must be converted to O-Mad2 for a functional checkpoint. Indeed, in cells that have a significant population of available O-Mad2, such as HeLa cells (Luo et al., 2004), TRIP13 function becomes essential for checkpoint activity only when this population of O-Mad2 is limiting (Ma and Poon, 2018). However, these results raise another question: if one of PCH-2's/TRIP13's role is to make enough O-Mad2 available for checkpoint activation, why does PCH-2/TRIP13 localize to unattached kinetochores (Nelson et al., 2015; Tipton et al., 2012; Wang et al., 2014)? One possible answer comes from our

bioRxiv preprint doi: https://doi.org/10.1101/389080; this version posted November 4, 2019. The copyright holder for this preprint (which was not certified by peer review) is the author/funder, who has granted bioRxiv a license to display the preprint in perpetuity. It is made available under aCC-BY 4.0 International license.

analysis of worms in which *cmt-1*, the *C. elegans* ortholog of p31^{comet}, has been mutated. In addition to its role as a PCH-2 adapter (Ye et al., 2015), CMT-1 is also required to localize PCH-2 to unattached kinetochores during the spindle checkpoint response, stabilize Mad2 protein levels and generate a robust spindle checkpoint response in AB cells (Nelson et al., 2015). Overexpressing Mad2 does not suppress the partial defect in spindle checkpoint activation in *cmt-1* mutants (Nelson et al., 2015), suggesting that PCH-2 localizes to unattached kinetochores to regulate spindle checkpoint strength.

Here, we test this possibility and show that PCH-2 controls spindle checkpoint strength in *C. elegans*. Despite being essential for the spindle checkpoint in the large somatic, or AB, cell of the two-cell embryo (Nelson et al., 2015), PCH-2 becomes dispensable for both the spindle checkpoint and Mad2 recruitment at unattached kinetochores as AB cells are genetically manipulated to become smaller. The requirement for PCH-2 in promoting spindle checkpoint strength is also observed in germline precursor, or P_1, cells, which have a stronger checkpoint than their somatic counterparts. PCH-2 is enriched in P_1 cells and this enrichment depends on a conserved regulator of embryonic polarity, PAR-1. Further, the stronger checkpoint in P_1 cells also relies on the *C. elegans* ortholog of p31^{comet}, CMT-1, indicating that CMT-1's ability to enrich PCH-2 in P_1 cells, in addition to its role in localizing PCH-2 to unattached kinetochores, contributes to a stronger checkpoint. We propose that PCH-2, and its mammalian ortholog TRIP13, ensure a robust spindle checkpoint response and proper chromosome segregation by regulating the availability of O-Mad2 at and near unattached kinetochores. This role may be specifically relevant in scenarios where maintaining genomic stability is particularly challenging, such as in oocytes and early embryos enlarged for developmental competence and germline cells that maintain immortality.

bioRxiv preprint doi: https://doi.org/10.1101/389080; this version posted November 4, 2019. The copyright holder for this preprint (which was not certified by peer review) is the author/funder, who has granted bioRxiv a license to display the preprint in perpetuity. It is made available under aCC-BY 4.0 International license.

RESULTS

PCH-2 becomes dispensable for the spindle checkpoint response in somatic cells experimentally reduced in size

In the large somatic, or AB, cell of the *C. elegans* two-cell embryo, PCH-2 is essential for spindle checkpoint activation (Nelson et al., 2015). To further assess the requirements for PCH-2 function, we manipulated the cell volume of AB cells experimentally by performing RNA interference (RNAi) against *ani-2*. *ani-2* encodes a germline specific anillin whose depletion generates oocytes and, after fertilization, embryos, of varying size (Maddox et al., 2005) (Figure 1A). We monitored the length of mitosis in these embryos, using the time between nuclear envelope breakdown (NEBD) to the onset of cortical contractility (OCC) as markers for the entry into and exit from mitosis, respectively (Essex et al., 2009). We then correlated the length of mitosis to cytoplasmic volume. RNAi of *ani-2* did not affect cell cycle progression in control, *pch-2*, or *mad-1* mutants (Figure S1A), indicating that reducing cytoplasmic volume did not affect mitotic timing in these embryos. (In *C. elegans*, the genes that encode Mad1 and Mad2 are *mdf-1* and *mdf-2*, respectively. To avoid confusion, we will use *mad-1* and *mad-2*).

We performed double depletion of *ani-2* and *zyg-1* to induce the spindle checkpoint response in control embryos, *pch-2*, and *mad-1* mutants. ZYG-1 is essential for centrosome duplication and after the first embryonic division, its depletion generates monopolar spindles (O'Connell et al., 2001) and unattached kinetochores (Essex et al., 2009) (Figure 1B). Consistent with previous reports, as cells decreased in cell volume the length of the cell cycle delay, an indicator of spindle checkpoint strength, increased in control embryos (Galli and Morgan, 2016; Gerhold et al., 2018) (Figure 1C, Videos 1 and 2). Surprisingly, as *pch-2* mutant embryos decreased in size, the spindle checkpoint

bioRxiv preprint doi: https://doi.org/10.1101/389080; this version posted November 4, 2019. The copyright holder for this preprint (which was not certified by peer review) is the author/funder, who has granted bioRxiv a license to display the preprint in perpetuity. It is made available under aCC-BY 4.0 International license.

response more closely resembled that of control embryos than *mad-1* mutant embryos (Figure 1C, Videos 3 and 4). There was no significant difference between the slopes of the regression analysis of control and *pch-2* mutant data (p value = 0.1407), while the slopes between the regression analysis of *pch-2* and *mad-1* mutant data were significantly different (p value = 0.0007). We partitioned our data to show that *pch-2* mutant embryos fell into three clear categories: 1) wild-type sized embryos (more than 5 x 10^3 μm^3) in which PCH-2 was essential for the spindle checkpoint; 2) medium sized embryos (between 3.5 x 10^3 μm^3 and 5 x 10^3 μm^3), which exhibited an intermediate level of checkpoint function; and 3) small embryos (less than 3.5 x 10^3 μm^3), in which PCH-2 was completely dispensable for the spindle checkpoint response (Figure 1D).

We verified that the mitotic delay observed in *pch-2* embryos was a legitimate spindle checkpoint response by monitoring mitotic timing after performing double depletion of *ani-2* and *zyg-1* in *san-1* and *pch-2;san-1* mutant embryos. SAN-1 is the *C. elegans* ortholog of the essential spindle checkpoint factor, Mad3 (Nystul et al., 2003) (Figure S1B). There was no significant difference between the slopes of the regression analysis of *san-1* and *pch-2;san-1* data (p value = 0.8813). These data allow us to draw two important conclusions: 1) Since we observe robust spindle checkpoint activation in *pch-2* mutant embryos as they decrease in size and mitotic timing is similar to what we observe in control embryos, PCH-2 does not appear to affect spindle checkpoint silencing in *C. elegans*; and 2) the requirement for PCH-2 during spindle checkpoint activation is proportional to cell volume in AB cells with monopolar spindles.

PCH-2 becomes dispensable for MAD-2 recruitment at unattached kinetochores in somatic cells experimentally reduced in size

bioRxiv preprint doi: https://doi.org/10.1101/389080; this version posted November 4, 2019. The copyright holder for this preprint (which was not certified by peer review) is the author/funder, who has granted bioRxiv a license to display the preprint in perpetuity. It is made available under aCC-BY 4.0 International license.

171 We showed that PCH-2 is required for robust recruitment of Mad2 at unattached
172 kinetochores during spindle checkpoint activation in AB cells of two-cell embryos
173 (Nelson et al., 2015). Therefore, we tested whether the checkpoint induced delay we
174 observed in small *ani-2*^{RNAi}*;zyg-1*^{RNAi}*;pch-2* embryos was accompanied by increased
175 recruitment of GFP::MAD-2 at unattached kinetochores. We quantified GFP::MAD-2
176 recruitment at unattached kinetochores in pseudo-metaphase in small control and *pch-2*
177 mutant embryos (less than 3.5 x 10^3 μm^3) and compared it to the recruitment observed
178 in wild-type sized embryos. Consistent with our previous results, GFP::MAD-2 was
179 recruited to 20% of control levels in *pch-2* mutant embryos that were wild-type in size
180 (Nelson et al., 2015) (Figures 2A and B). In small embryos, GFP::MAD-2 was recruited
181 to unattached kinetochores in control embryos as expected (Figure 2B). In small *pch-2*
182 mutant embryos, GFP::MAD-2 signal can be detected at unattached kinetochores
183 (Figure 2B) and, when quantified, GFP::MAD-2 was partially restored to 58% of control
184 levels (Figure 2B).
185
186 One explanation for why GFP::MAD-2 recruitment is not completely restored in small
187 *pch-2;ani-2*^{RNAi}*;zyg-1*^{RNAi} mutant embryos may be that these smaller embryos require
188 less MAD-2 recruitment to support a mitotic delay than control small embryos
189 (Defachelles et al., 2015). Consistent with this idea, when we plotted GFP::MAD-2
190 fluorescence against cell volume, we observed that the regression analysis of
191 GFP::MAD-2 fluorescence at unattached kinetochores in *pch-2;ani-2*^{RNAi}*;zyg-1*^{RNAi}
192 embryos exhibited a negative slope, showing improved GFP::MAD-2 recruitment to
193 unattached kinetochores as cells got smaller, but still lower in fluorescence intensity than
194 *ani-2*^{RNAi}*;zyg-1*^{RNAi} control embryos (Figure S2A). Surprisingly, the regression analysis for
195 control embryos had a positive slope, suggesting that less GFP::MAD-2 is required at
196 unattached kinetochores for spindle checkpoint function even in small control embryos

bioRxiv preprint doi: https://doi.org/10.1101/389080; this version posted November 4, 2019. The copyright holder for this preprint (which was not certified by peer review) is the author/funder, who has granted bioRxiv a license to display the preprint in perpetuity. It is made available under aCC-BY 4.0 International license.

(Figure S2A). This was despite similar levels of soluble GFP::MAD2 in both genetic backgrounds (Figure S2B). Nevertheless, our experiments demonstrate that PCH-2 is dispensable for Mad2 recruitment at unattached kinetochores in AB cells with monopolar spindles.

MAD-2 dosage controls checkpoint strength

MAD-2 is localized to the nucleus and nuclear envelope in *C. elegans* oocytes (Bohr et al., 2015; Lawrence et al., 2015) (Figure 3A). Since *ani-2*^{RNAi} treatment does not affect nuclear size (Figure S3), we reasoned that as cells are genetically manipulated to decrease in cell volume, the absolute amount of Mad2 protein is likely to remain constant but its concentration increases. This increase in concentration of Mad2, and O-Mad2 in particular, may obviate the requirement for PCH-2 in small embryos (Figure 3B).

To test this possibility, we initially attempted to directly visualize O-Mad2 in *C. elegans* embryos. Unfortunately, we were unable to perform this experiment with a commercial antibody (data not shown). Further, we could not directly probe total Mad2 concentration as cells decrease in volume upon treatment with *ani-2* RNAi because GFP::MAD-2 does not localize to the nucleus and instead localizes in the cytoplasm until NEBD (Essex et al., 2009; Nelson et al., 2015), making it an inaccurate reporter for this assay. Instead, we tested whether reducing Mad2 dosage affected checkpoint strength. We hypothesized that if Mad2 concentration influences checkpoint strength, reducing it by half should attenuate checkpoint strength in comparison to control animals. We performed double depletion of *ani-2* and *zyg-1* by RNAi in *mad-2* heterozygotes. Indeed, *mad-2* heterozygotes exhibited stronger spindle checkpoint strength as AB cells became smaller but not as robustly as control embryos (Figure 3C). The slopes of the linear regressions for both control and *mad-2* heterozygotes were significantly non-zero (p

bioRxiv preprint doi: https://doi.org/10.1101/389080; this version posted November 4, 2019. The copyright holder for this preprint (which was not certified by peer review) is the author/funder, who has granted bioRxiv a license to display the preprint in perpetuity. It is made available under aCC-BY 4.0 International license.

value = 0.0002 for control and p = .0395 for *mad-2/+*), unlike similar experiments with *mad-1* homozygotes (p value = 0.4197) (Figure 1B). Therefore, spindle checkpoint strength depends on MAD-2 dosage.

We wondered whether the decrease in Mad2 protein levels might restore the reliance on PCH-2 in small embryos. However, *pch-2;mad-2/+* double mutants exhibited a substantial decrease in the production and viability of embryos, preventing us from performing these experiments: *pch-2;mad-2/+* double mutants produced broods that were 14% of control animals and only 1% of these embryos were viable. Further, *pch-2;mad-2* double mutants could not be recovered from *pch-2;mad-2/+* mothers, a genetic interaction that we did not observe when we generated *pch-2;mad-1* double mutants (Bohr et al., 2015) or *pch-2;san-1* double mutants (Figure S1B). Thus, in addition to MAD-2 dosage controlling checkpoint strength, it collaborates with PCH-2 to promote *C. elegans* fertility and viability.

PCH-2 is required for the spindle checkpoint response during embryogenesis

During embryogenesis, cell volume decreases and spindle checkpoint strength increases (Galli and Morgan, 2016; Gerhold et al., 2018). Given our observation, that PCH-2 becomes dispensable as cell volume decreases in the AB cell of two-cell embryos, we assessed whether this also happens during normal embryogenesis.

We first performed this experiment in *perm-1*^{RNAi} embryos treated with nocodazole. Cells of the AB lineage in control embryos exhibited a longer mitotic delay in 16-cell than in 4-cell embryos (Figure 4A), verifying that the spindle checkpoint increases in strength as cells decrease in volume during embryogenesis (Galli and Morgan, 2016; Gerhold et al., 2018). As a control, we performed the same experiment in *san-1* mutants and did not

bioRxiv preprint doi: https://doi.org/10.1101/389080; this version posted November 4, 2019. The copyright holder for this preprint (which was not certified by peer review) is the author/funder, who has granted bioRxiv a license to display the preprint in perpetuity. It is made available under aCC-BY 4.0 International license.

detect a mitotic delay when these embryos were treated with nocodazole (Figure 4A). Consistent with the results that PCH-2 is required in small AB cells treated with nocodazole (Figure 3A), *pch-2* mutant embryos treated with nocodazole resembled *san-1* mutants (Figure 4A). Thus, as cells of the AB lineage naturally decrease in cell size during embryogenesis, PCH-2 is essential for the spindle checkpoint when microtubules are absent.

We also tested if a subtle increase in MAD-2 protein levels would suppress the spindle checkpoint defect in *pch-2* mutant embryos. The presence of a GFP::MAD-2 transgene, in addition to endogenous MAD-2, results in about 2.5 times more MAD-2 in worms. This slight overexpression generates a normal spindle checkpoint response in control AB cells and can bypass the requirement for checkpoint components MAD-3 or BUB-3 (Essex et al., 2009), but not PCH-2 (Nelson et al., 2015). We found that overexpression of MAD-2 in control and *pch-2* mutant 4- and 16-cell embryos treated with nocodazole behaved similarly as their counterparts with normal levels of MAD-2 (Figure 4B).

Given that we activated the spindle checkpoint activation in *ani-2*^{RNAi} embryos by generating monopolar spindles (Figures 1C and 3C), we also performed this experiment in embryos with monopolar spindles. We used a fast acting temperature sensitive allele of *zyg-1* (*zyg-1*^{ts}) (O'Rourke et al., 2011) to activate the spindle checkpoint in developing embryos with a variable number of cells. We shifted embryos at different stages of development, verified the appearance of monopolar spindles and measured mitotic timing from NEBD to DECON. In control *zyg-1*^{ts} mutant embryos, we observed a delay in mitotic timing in cells from the AB lineage and this delay only became marginally longer as embryos had more cells (Figure 4C), similar to previous reports (Gerhold et al., 2018). In stark contrast to our *ani-2*^{RNAi} experiments, the mitotic timing observed in *pch-*

bioRxiv preprint doi: https://doi.org/10.1101/389080; this version posted November 4, 2019. The copyright holder for this preprint (which was not certified by peer review) is the author/funder, who has granted bioRxiv a license to display the preprint in perpetuity. It is made available under aCC-BY 4.0 International license.

2;zyg-1^{ts} mutant embryos was reduced in comparison to *zyg-1*^{ts} embryos. Thus, similar to our results with embryos treated with nocodazole, PCH-2 is required for the spindle checkpoint as cells of the AB lineage naturally decrease in cell size during embryogenesis and when the checkpoint is activated by the presence of monopolar spindles. However, additional considerations may make direct comparisons between our *ani-2*^{RNAi}*;zyg-1* ^{RNAi} experiments and *zyg-1*^{ts} dividing embryos difficult (see Discussion).

PCH-2 is responsible for the stronger spindle checkpoint in the germline lineage

Cell fate is another important determinant of spindle checkpoint strength. In *C. elegans* embryos, the spindle checkpoint is stronger in germline precursor cells than similarly sized somatic counterparts (Galli and Morgan, 2016; Gerhold et al., 2018). However, as we observed with AB cells (Nelson et al., 2015), PCH-2 is essential for the spindle checkpoint in wildtype-sized P_1 cells (Figure S4A). Therefore, having established that PCH-2 becomes dispensable for the spindle checkpoint as two-cell embryos are genetically manipulated to become smaller (Figures 1C and D), we tested whether PCH-2 contributed to the stronger spindle checkpoint in P_1 cells of two-cell embryos treated with *ani-2* RNAi (Figures 5 and S4B). Consistent with other reports (Galli and Morgan, 2016; Gerhold et al., 2018), when we performed double depletion of *ani-2* and *zyg-1* in control embryos and monitored mitotic timing, we observed P_1 cells with similar volumes as AB cells exhibiting a longer cell cycle delay (Figures 5A and S4B, Videos 5 and 6). Further, the regression analysis that best fit control P_1 data is significantly different and steeper than that of control AB cells (p value < 0.0001), indicating that variables in addition to cell volume contribute to the spindle checkpoint strength in germline precursor cells. When we knocked down both *ani-2* and *zyg-1* in *pch-2* mutant embryos, we no longer observed a significant difference (p value = 0.9096) between the slopes of

bioRxiv preprint doi: https://doi.org/10.1101/389080; this version posted November 4, 2019. The copyright holder for this preprint (which was not certified by peer review) is the author/funder, who has granted bioRxiv a license to display the preprint in perpetuity. It is made available under aCC-BY 4.0 International license.

the regression analysis of P_1 and AB cells (Figures 5B and S4B, Videos 7 and 8), indicating that PCH-2 is responsible for the stronger checkpoint in P_1 cells.

We observed that cell cycle timing was faster in *pch-2* mutant P_1 cells than similarly sized *pch-2* mutant AB cells after treatment with *ani-2* and *zyg-1* RNAi (Figures 5B and S4B). We wondered if embryonic germline precursor cells might rely on some spindle checkpoint proteins for normal mitotic timing, analogous to mitotically dividing stem cells in the *C. elegans* germline (Gerhold et al., 2015) and similar to mammalian cultured cells (Ma and Poon, 2016; Meraldi et al., 2004; Rodriguez-Bravo et al., 2014). To address this, we measured normal mitotic timing in AB and P_1 cells of both control and *pch-2* mutant embryos. We found that while normal mitotic timing is unaffected by mutation of *pch-2* in AB cells, *pch-2* mutant P_1 cells go through mitosis significantly faster than control P_1 cells (Figure 5C), thus providing an explanation for the faster cell cycle timing in *pch-2* mutant P_1 cells with the same cell volume as *pch-2* mutant AB cells after treatment with *ani-2* and *zyg-1* RNAi. We saw a decrease in the cell cycle timing of P_1 cells in *mad-1* mutants but this was not statistically different than control P_1 cells (Figure 5C).

PCH-2's enrichment in P_1 cells depends on PAR-1

Cell fate is driven by the asymmetric distribution of various determinants between somatic and germline lineages during early divisions of the *C. elegans* embryo (Rose and Gonczy, 2014). Since we found that PCH-2 promoted the spindle checkpoint strength in both AB and P_1 cells, but even more dramatically in P_1 cells, we asked if PCH-2 was regulated differently between these cells. First, we tested whether PCH-2::GFP could also support the stronger checkpoint in P_1 cells. We treated embryos

bioRxiv preprint doi: https://doi.org/10.1101/389080; this version posted November 4, 2019. The copyright holder for this preprint (which was not certified by peer review) is the author/funder, who has granted bioRxiv a license to display the preprint in perpetuity. It is made available under aCC-BY 4.0 International license.

expressing PCH-2::GFP with *zyg-1* RNAi and evaluated mitotic timing in both AB and P_1 cells, in the presence or absence of monopolar spindles, using chromosome decondensation as a marker for mitotic exit. P_1 cells expressing PCH-2::GFP had full checkpoint function, exhibiting a mitotic delay longer than AB cells also expressing PCH-2::GFP (Figure 6A).

Previous transcriptome analysis of PCH-2 did not reveal asymmetric enrichment of PCH-2 mRNA between AB and P_1 cells (Tintori et al., 2016). We tested whether PCH-2::GFP exhibited differences in protein levels between AB and P_1 cells. First, we assessed whether PCH-2::GFP was more enriched in pseudo-metaphase at unattached kinetochores in P_1 than AB cells. We quantified PCH-2::GFP fluorescence at unattached kinetochores in both AB and P_1 cells of embryos treated with *zyg-1* RNAi but did not detect any difference between the two cell types (Figures S5A and B). Similarly, we did not detect any difference in GFP::MAD-2 recruitment at unattached kinetochores between AB and P_1 cells in *zyg-1*^{RNAi} embryos (Figures S5C and D).

Since neither PCH-2::GFP or GFP::MAD-2 recruitment to unattached kinetochores were different between AB and P_1 cells (Figure S5) and given the existence of a “cloud” of checkpoint factors, including MAD-2 and PCH-2, around chromosomes, even during normal cell cycles (Essex et al., 2009; Nelson et al., 2015), we quantified PCH-2::GFP fluorescence around mitotic chromosomes in AB and P_1 cells during unperturbed cell cycles. Similar to AB cells (Nelson et al., 2015), we observed PCH-2::GFP enriched in the area around the chromosomes in prometaphase in P_1 cells (Figure 6B). When we quantified the fluorescence of PCH-2::GFP in this area surrounding chromosomes after NEBD in both AB and P_1 cells, we detected a statistically significant enrichment of PCH-2::GFP in P_1 cells (Figure 6C). To evaluate whether this enrichment was the indirect

bioRxiv preprint doi: https://doi.org/10.1101/389080; this version posted November 4, 2019. The copyright holder for this preprint (which was not certified by peer review) is the author/funder, who has granted bioRxiv a license to display the preprint in perpetuity. It is made available under aCC-BY 4.0 International license.

consequence of the smaller volume of P_1 cells, we also quantified PCH-2::GFP fluorescence in *gpr-1/2*^{RNAi} embryos. This double knockdown equalizes the size of AB and P_1 cells without affecting their cell fate (Colombo et al., 2003; Gotta et al., 2003; Srinivasan et al., 2003). *gpr-1/2*^{RNAi} embryos showed a similar enrichment of PCH-2::GFP in P_1 cells as control embryos (Figure S7).

To better understand the relationship between PCH-2 enrichment in P_1 cells and cell fate, we abrogated the asymmetry of the two-cell embryo by performing RNAi against the essential polarity factor, PAR-1 (Guo and Kemphues, 1995). In *par-1*^{RNAi} mutant embryos, both AB and P_1 cells exhibit the same checkpoint strength as control P_1 cells (Gerhold et al., 2018), indicating that the stronger spindle checkpoint response in the P_1 cells depends on this asymmetric division. Despite the loss of cell fate in *par-1*^{RNAi} embryos, we will refer to the anterior blastomere as AB and the posterior as P_1. We quantified PCH-2::GFP fluorescence in the area around chromosomes in AB and P_1 cells after *par-1* RNAi and observed that the fluorescence of PCH-2::GFP, despite being slightly lower in P_1 cells, was not significantly different between AB and P_1 cells, unlike what we observed in embryos exposed to control RNAi (Figures 6D and E). Further, similar to the effect on spindle checkpoint strength (Gerhold et al., 2018), we found that the concentration of PCH-2::GFP in *par-1*^{RNAi} AB cells was greater than that of control AB cells (data not shown) and more closely resembled PCH-2::GFP concentration in P_1 cells treated with control RNAi (p value = 0.348). Therefore, PCH-2::GFP's enrichment around mitotic chromosomes in P_1 cells depends on a conserved factor that induces embryonic asymmetry and germline cell fate, PAR-1.

The stronger checkpoint in P_1 cells depends on CMT-1

bioRxiv preprint doi: https://doi.org/10.1101/389080; this version posted November 4, 2019. The copyright holder for this preprint (which was not certified by peer review) is the author/funder, who has granted bioRxiv a license to display the preprint in perpetuity. It is made available under aCC-BY 4.0 International license.

In vitro, the *C. elegans* ortholog of p31^{comet}, CMT-1, is required for PCH-2 to bind and remodel Mad2 (Ye et al., 2015). In addition to this role, CMT-1 is also required to localize PCH-2 to unattached kinetochores and generate a robust spindle checkpoint response in AB cells (Nelson et al., 2015). Therefore, we reasoned that CMT-1 might also be required for the stronger checkpoint in P_1 cells.

To test this possibility, we first performed double knockdown of *ani-2* and *zyg-1* in *cmt-1* mutants and monitored the length of the spindle checkpoint response as AB and P_1 cells became smaller (Figure 7A, Videos 9-12). Similar to *pch-2;ani-2^{RNAi};zyg-1^{RNAi}* mutants (Figure 5B), the stronger spindle checkpoint response in P_1 cells was lost in *cmt-1;ani-2^{RNAi};zyg-1^{RNAi}* mutants and we did not observe any statistical difference between the between the slopes of the regression analysis of P_1 and AB cells (p value = 0.9403). We also observed that cell cycle timing was faster in *cmt-1* P_1 cells that were similar in volume to *cmt-1* AB cells. Thus, CMT-1 is also essential to promote spindle checkpoint strength in germline precursor cells.

We also performed *zyg-1* RNAi on control and *cmt-1* mutant embryos and monitored mitotic timing in both AB and P_1 cells. AB and P_1 cells of control and *cmt-1* mutant embryos treated with control RNAi had similar mitotic timing. Unlike similar experiments in *pch-2* mutants (Figure 5C), we did not detect a statistically significant difference between cell cycle time in P_1 cells between wildtype and *cmt-1* mutants embryos (Figure 7B), suggesting that *ani-2^{RNAi};zyg-1^{RNAi}* embryos might be more sensitive to subtle perturbations in cell cycle timing. In *zyg-1^{RNAi}* embryos, P_1 cells exhibited a stronger checkpoint response than AB cells (Figure 7B). By contrast, both AB and P_1 cells in *cmt-1;zyg-1^{RNAi}* mutant embryos exhibited similar spindle checkpoint delays (Figure 7B).

bioRxiv preprint doi: https://doi.org/10.1101/389080; this version posted November 4, 2019. The copyright holder for this preprint (which was not certified by peer review) is the author/funder, who has granted bioRxiv a license to display the preprint in perpetuity. It is made available under aCC-BY 4.0 International license.

Despite having spindle checkpoint responses that were less robust than that of control *zyg-1*^{RNAi} embryos, AB and P_1 cells in *cmt-1* mutant embryos treated with *zyg-1* RNAi spent significantly longer in mitosis than *cmt-1* mutant embryos treated with control RNAi (Figure 7B), indicating that they activated a weaker spindle checkpoint response, similar to our published results (Nelson et al., 2015). More importantly, *cmt-1*;*zyg-1*^{RNAi} mutant embryos failed to generate a stronger checkpoint in P_1 cells, consistent with *cmt-1;ani-2*^{RNAi}*;zyg-1*^{RNAi} experiments (Figure 7A).

Aside from localizing PCH-2 to unattached kinetochores (Nelson et al., 2015), we wondered if CMT-1 was required for any other aspects of PCH-2 regulation. Therefore, we tested whether CMT-1 was necessary for PCH-2's asymmetric enrichment in P_1 cells. We quantified PCH-2::GFP fluorescence in prometaphase in the area around chromosomes in both *cmt-1* mutant AB and P_1 cells (Figure 7C). First, we found that PCH-2::GFP fluorescence was slightly higher in AB cells in *cmt-1* mutants than control embryos (Figure 7D). We saw a similar result in our *par-1* RNAi experiments (data not shown), although in both cases these increases were not statistically significant. However, unlike *par-1*^{RNAi} embryos (Gerhold et al., 2018), this increase in PCH-2::GFP was not accompanied by an increase in checkpoint strength (Figure 7B), consistent with our hypothesis that the weaker checkpoint in *cmt-1* AB cells is a consequence of PCH-2's absence from unattached kinetochores (Nelson et al., 2015). Further, when we compared the quantification of PCH-2::GFP fluorescence in *cmt-1* mutant AB and P_1 cells, we did not detect a significant difference between the two cells (Figure 7E), unlike our experiment in control embryos (Figures 6B and C), indicating that CMT-1 contributes to the asymmetric enrichment of PCH-2 in P_1 cells. Thus, CMT-1 promotes spindle checkpoint strength through two mechanisms: localizing PCH-2 to unattached kinetochores and ensuring its enrichment in germline precursor cells.

bioRxiv preprint doi: https://doi.org/10.1101/389080; this version posted November 4, 2019. The copyright holder for this preprint (which was not certified by peer review) is the author/funder, who has granted bioRxiv a license to display the preprint in perpetuity. It is made available under aCC-BY 4.0 International license.

DISCUSSION

The role of PCH-2, and its mammalian ortholog TRIP13, in the spindle checkpoint has been enigmatic. Originally identified as a checkpoint silencing factor (Alfieri et al., 2018; Brulotte et al., 2017; Eytan et al., 2014; Miniowitz-Shemtov et al., 2015; Wang et al., 2014; Ye et al., 2015), more recent evidence also indicates a role in promoting the checkpoint response (Ma and Poon, 2016; Ma and Poon, 2018; Nelson et al., 2015; Yost et al., 2017). It's clear that the reliance on PCH-2/TRIP13 in checkpoint activation reflects the relative levels and availability of O-Mad2 (Ma and Poon, 2018). We show here that PCH-2 also controls checkpoint strength. We propose that PCH-2 accomplishes this by regulating O-Mad2 availability, specifically at and near unattached kinetochores, providing an unanticipated mechanism to explain checkpoint strength (Figure 8). This role in checkpoint strength may be particularly important in large cells, such as oocytes and cells in early embryos, as well as cells that give rise to immortal germ cells.

Our model assumes that two cell embryos have a significant amount of O-Mad2 available, even when PCH-2 function is lost (Figure 8), unlike what is reported in mammalian cells (Ma and Poon, 2016). Given that this is a developmental system in which embryos have only undergone a single mitotic division before we perform our assays, we propose that O-Mad2 is not limiting in very early embryos, even in *pch-2* null mutants. In this way, *C. elegans* two-cell embryos would be analogous to mammalian cells undergoing cell division soon after acute depletion of TRIP13 (Ma and Poon, 2018). Unfortunately, we were unable to directly probe O-Mad2 concentration or its availability at or near unattached kinetochores in small *ani-2*^{RNAi} embryos or germline precursor

bioRxiv preprint doi: https://doi.org/10.1101/389080; this version posted November 4, 2019. The copyright holder for this preprint (which was not certified by peer review) is the author/funder, who has granted bioRxiv a license to display the preprint in perpetuity. It is made available under aCC-BY 4.0 International license.

453 cells. However, we think that several pieces of data support this hypothesis: PCH-2's
454 characterized biochemical activity converts C-Mad2 to O-Mad2 (Alfieri et al., 2018;
455 Brulotte et al., 2017; Ye et al., 2015); an inability to localize and/or enrich PCH-2 at and
456 around unattached kinetochores affects checkpoint strength (Nelson et al., 2015;
457 Gerhold et al., 2018 and Figures 6 and 7); the delay we observe in small *pch-2;ani-*
458 *2*^{RNAi}*;zyg-1*^{RNAi} embryos is checkpoint dependent (Figure S1B); as cells are genetically
459 manipulated to become smaller, robust checkpoint strength depends on Mad2 dosage
460 (Figure 2C); GFP::MAD-2 localization is restored to unattached kinetochores in small
461 *pch-2;ani-2*^{RNAi}*;zyg-1*^{RNAi} embryos (Figures 2D and E); and *pch-2* and *mad-2* mutant
462 alleles genetically interact, indicating a close functional relationship between these two
463 genes during embryogenesis.
464
465 Another prediction of our model is that overexpression of Mad2 should also make PCH-2
466 dispensable for spindle checkpoint activation. We've shown that subtle elevations of
467 Mad2 protein levels cannot suppress the requirement for PCH-2 in two-cell embryos
468 (Nelson et al., 2015). Unfortunately, more dramatic overexpression experiments are
469 technically difficult in *C. elegans*. Further, it's likely that strong overexpression of Mad2 in
470 *C. elegans* embryos will delay normal mitosis, consistent with similar findings in
471 mammalian cells (Marks et al., 2017) and budding yeast (Mariani et al., 2012). In this
472 way, PCH-2's function may provide a useful buffer: Since Mad2 protein levels may need
473 to stay within a narrow range to allow normal mitotic timing, PCH-2's localization at and
474 near unattached kinetochores provide a mechanism to increase O-Mad2's local
475 concentration to promote effective and efficient signaling during checkpoint activation.
476
477 Despite our findings that PCH-2 becomes dispensable for spindle checkpoint activation
478 as two-cell embryos are experimentally induced to decrease in volume, PCH-2 remains

bioRxiv preprint doi: https://doi.org/10.1101/389080; this version posted November 4, 2019. The copyright holder for this preprint (which was not certified by peer review) is the author/funder, who has granted bioRxiv a license to display the preprint in perpetuity. It is made available under aCC-BY 4.0 International license.

479 essential for the spindle checkpoint as AB cells normally decrease in volume during
480 embryogenesis (Figure 4). This inconsistency could be explained by a variety of
481 reasons. O-Mad2 may eventually become limiting in cells of the AB lineage with
482 successive divisions after the two-cell stage, resulting in a greater reliance on PCH-2
483 function. Moreover, it may also suggest that relative levels of O-Mad2 and C-Mad2 are
484 more stringently regulated as embryonic development progresses and the multi-cellular
485 embryo becomes more complex. This possibility is supported by our finding that PCH-2
486 regulates normal cell cycle timing in P_1 cells, but not AB cells (Figure 5C), which implies
487 that variations in O-Mad2/C-Mad2 ratios influence normal mitotic timing in cells with
488 specific developmental fates. In addition, unlike the nuclei of two-cell embryos treated
489 with *ani-2*^{RNAi} (Figure S3), nuclear volume scales with cell volume during embryogenesis
490 (Gerhold et al., 2018). Therefore, the concentration of Mad2 may not necessarily
491 increase as cell size decreases in cells of the developing embryo, making direct
492 comparisons between small cells obtained by *ani-2*^{RNAi} treatment and small cells
493 resulting from normal embryogenesis challenging. Finally, recent reports have indicated
494 that, during embryogenesis in other systems, cell volume may not be a major contributor
495 to spindle checkpoint strength (Chenevert et al., 2019; Vazquez-Diez et al., 2019).
496 Indeed, in *C. elegans*, when only AB cells are monitored during early embryogenesis,
497 they exhibit very minor increases, if any, in checkpoint strength (Galli and Morgan, 2016;
498 Gerhold et al., 2018 and Figure 4). This may suggest that cell fate is generally a more
499 important determinant of spindle checkpoint strength during normal embryogenesis,
500 potentially reconciling reports from a wide array of systems.
501
502 Our experiments identify CMT-1, the *C. elegans* ortholog of mammalian p31^{comet}, as an
503 important regulator of PCH-2 function and, as a result, checkpoint strength. In addition to
504 its requirement in facilitating PCH-2's ability to interact with its substrate, Mad2 (Alfieri et

bioRxiv preprint doi: https://doi.org/10.1101/389080; this version posted November 4, 2019. The copyright holder for this preprint (which was not certified by peer review) is the author/funder, who has granted bioRxiv a license to display the preprint in perpetuity. It is made available under aCC-BY 4.0 International license.

al., 2018; Brulotte et al., 2017; Miniowitz-Shemtov et al., 2015; Ye et al., 2015), CMT-1 localizes PCH-2 to unattached kinetochores (Nelson et al., 2015) and promotes PCH-2's enrichment in P_1 cells (Figure 7). We propose that both of these roles contribute to checkpoint strength. In large AB cells, CMT-1 ensures PCH-2's presence at unattached kinetochores, increasing the local concentration of O-Mad2, driving the production of soluble C-Mad2 and MCC and enforcing a robust checkpoint (Figure 8A). In P_1 cells, the combination of PCH-2's localization at kinetochores and its enrichment around chromosomes and near unattached kinetochores produces a checkpoint stronger than somatic cells (Figure 8C). It's striking that, when CMT-1 is absent, AB cells, in which there is more PCH-2 (Figure 7D), and P_1 cells, which are slightly smaller than AB cells, exhibit similar checkpoint strength (Figure 7B). This indicates that even these cells depend on PCH-2 to be present at unattached kinetochores to increase the local concentration of O-Mad2 and promote checkpoint strength.

P_1 cells in both *pch-2;ani-2*^{RNAi}*;zyg-1*^{RNAi} and *cmt-1;ani-2*^{RNAi}*;zyg-1*^{RNAi} mutants show faster cell cycle timing than similarly sized AB cells of the same genotype (Figures 5B and 7A). However, only *pch-2* mutants significantly affect cell cycle timing in unperturbed P_1 cells, (Figure 5C); P_1 cells in *cmt-1* and *mad-1* mutants show accelerated cell cycle timing but this is not significantly faster than control (Figures 5C and 7B). Given the rapidity of cell cycles in these early embryos, it's possible that *ani-2*^{RNAi}*;zyg-1*^{RNAi} experiments provide greater sensitivity to observe subtle accelerations in cell cycle timing and that some subset of spindle checkpoint components, including PCH-2, CMT-1, MAD-1 and MAD-2 regulate normal cell cycle timing in germline precursor cells, similar to the role of MAD-1 and MAD-2 in germline mitotic nuclei (Gerhold et al., 2015). An alternative hypothesis that we do not favor is that only PCH-2 regulates cell cycle timing in P_1 cells, in a mechanism independent of other spindle checkpoint proteins.

bioRxiv preprint doi: https://doi.org/10.1101/389080; this version posted November 4, 2019. The copyright holder for this preprint (which was not certified by peer review) is the author/funder, who has granted bioRxiv a license to display the preprint in perpetuity. It is made available under aCC-BY 4.0 International license.

Evolutionary analysis across phyla have revealed a close co-evolutionary relationship between PCH-2 and its orthologs and HORMA domain containing proteins, including CMT-1 and Mad2 (van Hooff et al., 2017; Vleugel et al., 2012). However, some organisms that rely on the templated conversion of O-Mad2 to C-Mad2 to assemble the MCC, such as budding and fission yeasts (Chao et al., 2012; Nezi et al., 2006) either don't express their PCH-2 ortholog during mitosis (budding yeast) (San-Segundo and Roeder, 1999) or don't have a PCH-2 ortholog in their genome (fission yeast) (Wu and Burgess, 2006). This is potentially explained by cell volume: Both budding and fission yeasts are two orders of magnitude smaller than mammalian cells and *C. elegans* embryos. They also undergo closed mitosis, in which the nuclear envelope does not break down, providing an additional opportunity to concentrate factors required for mitosis. We propose that recruiting O-Mad2 to unattached kinetochores may not present as great a challenge in these significantly smaller cells, making a factor required to increase the local concentration of O-Mad2 at unattached kinetochores unnecessary.

An obvious question our experiments raise is how PCH-2 is enriched in P_1 cells. Germline precursor cells are transcriptionally silent until gastrulation (Seydoux et al., 1996) and sequencing of mRNA in early embryos shows that both CMT-1 and PCH-2 mRNA are not enriched in germline precursor cells (Tintori et al., 2016), indicating that enrichment of PCH-2 is likely to occur at the level of protein regulation. Understanding this regulation, its control by developmental events and its effect on the relative levels of O-Mad2 and C-Mad2 in different cell types promises to be an exciting area of investigation.

MATERIALS AND METHODS

bioRxiv preprint doi: https://doi.org/10.1101/389080; this version posted November 4, 2019. The copyright holder for this preprint (which was not certified by peer review) is the author/funder, who has granted bioRxiv a license to display the preprint in perpetuity. It is made available under aCC-BY 4.0 International license.

Worms strains

The *C. elegans* Bristol N2 (Brenner, 1974) was used as the wild-type strain. Most strains were maintained at 20°C, except for *zyg-1(or297)* strains, which were maintained at 15°C. See Table S1 for the list of all the strains used in this study.

Immunostaining

Immunostaining was performed on adult worms 48h after L4, as described in (Bhalla and Dernburg, 2005). The antibodies used were rabbit anti-MAD-2 (1/500; (Essex et al., 2009) and mouse anti-MAb414 (1/400; (Davis and Blobel, 1986). Secondary antibodies were Alexa Fluor 488 anti-rabbit (Invitrogen) and Cy3 anti-mouse (Jackson ImmunoResearch Laboratories, Inc.) diluted at 1:500. Antibody against MAD-2 was a gift from A. Desai (Ludwig Institute/University of California, San Diego, La Jolla, CA).

Images were acquired on a DeltaVision Personal DV microscope (GE Healthcare) equipped with a 100× NA 1.40 oil-immersion objective (Olympus), a short ARC xenon lamp (GE Healthcare) and using a CoolSNAP charge-coupled camera (Roper Scientific). Z-stacks were collected at 0.2 µm Z-spacing and processed by constrained, iterative deconvolution. Imaging, image scaling, and analysis were performed using functions in the softWoRx software package (GE Healthcare). Projections were calculated by a maximum intensity algorithm. Composite images were assembled and some false coloring was performed with Fiji.

Live imaging of two-cell embryos

For live imaging of two-cell embryos, worms were dissected on glass coverslips in egg buffer and then mounted on 2% agar pads. Images were acquired every 1 minute or 20

bioRxiv preprint doi: https://doi.org/10.1101/389080; this version posted November 4, 2019. The copyright holder for this preprint (which was not certified by peer review) is the author/funder, who has granted bioRxiv a license to display the preprint in perpetuity. It is made available under aCC-BY 4.0 International license.

seconds on a DeltaVision Personal DV microscope as described in the previous section; except that the distance between two planes was 2 µm. Mitotic timing was measured from NEBD to OCC as described in (Nelson et al., 2015). Cell volumes were measured as described in (Galli and Morgan, 2016). To measure the nuclear area, a sum projection of the embryo was generated 1 minute before chromosomes began to condense and the area was measured with Fiji (Figure S2A).

Live imaging of embryogenesis

After treatment with *perm-1*^{RNAi} (see below), worms were dissected onto a coverslip with egg salt buffer (118 mM NaCl, 48 mM KCl) supplemented with 10 mM PIPES pH 7.3, 1 mM ATP and 10 mM sucrose. Embryos and adult carcasses were transferred into a well of an 8-well plate (ibidi 1 µ-Slide 8 Well Glass bottom) that had been freshly coated with 0.1% Poly-L-Lysine solution (Sigma P8920) and extensively washed. Time-lapse videos were acquired with a Solamere spinning disk confocal system piloted by µManager software (Edelstein et al., 2014) and equipped with a Yokogawa CSUX-1 scan head, a Nikon (Garden City, NY) TE2000-E inverted stand, a Hamamatsu ImageEM ×2 camera, LX/MAS 489 nm and LS/MAS 561 nm laser, and Plan Apo ×60/1.4 numerical aperture oil objective. Acquisition times per frame were 50 ms using 5% of the lasers power for both channels, and images were obtained as stacks of planes at 2 µm intervals taken every 1 minute. Nocodazole was added from a 5X stock to a final concentration of 50 µM after the first time point. Mitotic timing was measured from NEBD to DECON as described in (Essex et al., 2009).

To image embryogenesis in *zyg-1(or297)* mutants, images were generated under the same conditions as previously described for the live imaging of two-cell embryos with a few modifications: Images were acquired every 20 seconds on a DeltaVision Personal

bioRxiv preprint doi: https://doi.org/10.1101/389080; this version posted November 4, 2019. The copyright holder for this preprint (which was not certified by peer review) is the author/funder, who has granted bioRxiv a license to display the preprint in perpetuity. It is made available under aCC-BY 4.0 International license.

DV microscope in a room heated to 26°C. Mitotic timing was measured from NEBD to DECON as described in (Essex et al., 2009).

Quantification of fluorescence intensity

To quantify GFP::MAD-2 and PCH-2::GFP levels, images were generated under the same conditions as previously described for the live imaging of two-cell embryos with a few modifications: only the nucleus was imaged, the interval between the four planes was 1 µm and images were collected every 20 seconds. Quantification of fluorescence at kinetochores was performed in Fiji as described in (Moyle et al., 2014; Nelson et al., 2015) and fluorescence in the cytoplasm as described in (Galli and Morgan, 2016). In some of our movies, identifying a clear metaphase plate was more difficult in AB than P_1 cells. Therefore, to ensure that we were quantifying PCH-2::GFP fluorescence around mitotic chromosomes at the same stage in mitosis in these two cell types, PCH-2::GFP was quantified in frames that were normalized relative to NEBD and mitotic exit. Sum intensity projections were generated and fluorescence in the area around mitotic chromosomes was measured in Fiji. Background fluorescence was measured in a 30 pixel band around this “cloud” and subtracted from the initial fluorescence intensity to determine the final fluorescence value. To measure the cell volume, one Z-stack of the entire cell was taken at NEBD at 2 µm Z-spacing.

Feeding RNA interference (RNAi)

C. elegans strains were fed HT115 bacteria expressing the desired dsRNA after IPTG induction. Bacterial strains containing RNAi vectors were cultured overnight at 37°C, centrifuged, and the pellet was resuspended in 1/50 of the original volume. 100 µl of concentrated culture was spotted onto a nematode growth medium (NGM) plate

bioRxiv preprint doi: https://doi.org/10.1101/389080; this version posted November 4, 2019. The copyright holder for this preprint (which was not certified by peer review) is the author/funder, who has granted bioRxiv a license to display the preprint in perpetuity. It is made available under aCC-BY 4.0 International license.

containing 1 mM IPTG and 50 µg/µl of kanamycin or carbenicillin and the plate was incubated overnight at 37°C.

For *ani-2* RNAi, gravid adults were bleached onto the RNAi plate and their progeny was allowed to develop at 20°C during 2.5 days. Then, L4s were transferred to a fresh plate containing OP50 or *zyg-1* RNAi bacteria.

For *zyg-1* RNAi, L4s were transferred (from an OP50 or *ani-2* RNAi plate) onto a *zyg-1* RNAi plate and cultured 1.5 days at 20°C.

For *perm-1* RNAi, young adults (8h post L4) were incubated onto *perm-1* RNAi plates for 16-20 hours at 15°C.

For *par-1* and *gpr-1/2* RNAi, gravid adults were bleached onto control RNAi (L4440) plates and their progeny were allowed to develop at 15°C for 3 days. L4s were then transferred onto *par-1, gpr-1/2* RNAi or control RNAi plates and incubated at 15°C for 3 days.

Statistical Analysis

Linear regression analysis and assessing significance of this data (Figures 1C, 3C, 5A, 5B, 7A, S1C, S1D, S2A, S4B) was performed using GrapPad Prism version 6 for Macintosh. For all other data, significance was assessed by performing t-tests (Figures 1D, 2B, 3C, 3D, 3E, 4A, 4B, 4C, 5C, 6A, 6C, 6E, 7B, 7D, 7E, S4A, S5B, S5D, S6B and S7C). In all graphs, a * indicates a p value < 0.05, ** indicates a p value < 0.01 and *** a p value < 0.0001.

bioRxiv preprint doi: https://doi.org/10.1101/389080; this version posted November 4, 2019. The copyright holder for this preprint (which was not certified by peer review) is the author/funder, who has granted bioRxiv a license to display the preprint in perpetuity. It is made available under aCC-BY 4.0 International license.

ACKNOWLEDGEMENTS

We would like to thank Arshad Desai, Karen Oegema, Susan Strome and David Morgan for valuable strains and reagents. This work was supported by the NIH (grant numbers T32GM008646 [C.R.N. and A.R.] and R01GM097144 [N.B.]). Some strains were provided by the CGC, which is funded by NIH Office of Research Infrastructure Programs (P40 OD010440).

CONTRIBUTIONS

Conceptualization and Methodology, L.D., A.E.R., C.R.N. and N.B.; Investigation, L.D., A.E.R., and C.R.N.; Writing - Original Draft, L.D. and N.B.; Writing - Review & Editing, L.D., A.E.R., C.R.N. and N.B.; Supervision and Funding Acquisition, N.B.

COMPETING INTERESTS

The authors declare no competing interests.

bioRxiv preprint doi: https://doi.org/10.1101/389080; this version posted November 4, 2019. The copyright holder for this preprint (which was not certified by peer review) is the author/funder, who has granted bioRxiv a license to display the preprint in perpetuity. It is made available under aCC-BY 4.0 International license.

REFERENCES

Alfieri, C., L. Chang, and D. Barford. 2018. Mechanism for remodelling of the cell cycle checkpoint protein MAD2 by the ATPase TRIP13. *Nature*. 559:274-278.

Aravind, L., and E.V. Koonin. 1998. The HORMA domain: a common structural denominator in mitotic checkpoints, chromosome synapsis and DNA repair. *Trends Biochem Sci*. 23:284-286.

Bhalla, N., and A.F. Dernburg. 2005. A conserved checkpoint monitors meiotic chromosome synapsis in Caenorhabditis elegans. *Science*. 310:1683-1686.

Bohr, T., C.R. Nelson, E. Klee, and N. Bhalla. 2015. Spindle assembly checkpoint proteins regulate and monitor meiotic synapsis in C. elegans. *J Cell Biol*. 211:233-242.

Brenner, S. 1974. The genetics of Caenorhabditis elegans. *Genetics*. 77:71-94.

Brulotte, M.L., B.C. Jeong, F. Li, B. Li, E.B. Yu, Q. Wu, C.A. Brautigam, H. Yu, and X. Luo. 2017. Mechanistic insight into TRIP13-catalyzed Mad2 structural transition and spindle checkpoint silencing. *Nat Commun*. 8:1956.

Chao, W.C., K. Kulkarni, Z. Zhang, E.H. Kong, and D. Barford. 2012. Structure of the mitotic checkpoint complex. *Nature*. 484:208-213.

Chen, R.H., A. Shevchenko, M. Mann, and A.W. Murray. 1998. Spindle checkpoint protein Xmad1 recruits Xmad2 to unattached kinetochores. *J Cell Biol*. 143:283-295.

Chen, R.H., J.C. Waters, E.D. Salmon, and A.W. Murray. 1996. Association of spindle assembly checkpoint component XMAD2 with unattached kinetochores. *Science*. 274:242-246.

Chenevert, J., M. Roca, L. Besnardeau, A. Ruggiero, D. Nabi, A. McDougall, R.R. Copley, E. Christians, and S. Castagnetti. 2019. The spindle assembly

bioRxiv preprint doi: https://doi.org/10.1101/389080; this version posted November 4, 2019. The copyright holder for this preprint (which was not certified by peer review) is the author/funder, who has granted bioRxiv a license to display the preprint in perpetuity. It is made available under aCC-BY 4.0 International license.

checkpoint functions during early development in non-chordate embryos. *bioRxiv*.

Collin, P., O. Nashchekina, R. Walker, and J. Pines. 2013. The spindle assembly checkpoint works like a rheostat rather than a toggle switch. *Nat Cell Biol*. 15:1378-1385.

Colombo, K., S.W. Grill, R.J. Kimple, F.S. Willard, D.P. Siderovski, and P. Gonczy. 2003. Translation of polarity cues into asymmetric spindle positioning in Caenorhabditis elegans embryos. *Science*. 300:1957-1961.

Davis, L.I., and G. Blobel. 1986. Identification and characterization of a nuclear pore complex protein. *Cell*. 45:699-709.

De Antoni, A., C.G. Pearson, D. Cimini, J.C. Canman, V. Sala, L. Nezi, M. Mapelli, L. Sironi, M. Faretta, E.D. Salmon, and A. Musacchio. 2005. The Mad1/Mad2 complex as a template for Mad2 activation in the spindle assembly checkpoint. *Current biology : CB*. 15:214-225.

Defachelles, L., S.G. Hainline, A. Menant, L.A. Lee, and R.E. Karess. 2015. A maternal effect rough deal mutation suggests that multiple pathways regulate Drosophila RZZ kinetochore recruitment. *J Cell Sci*. 128:1204-1216.

Dick, A.E., and D.W. Gerlich. 2013. Kinetic framework of spindle assembly checkpoint signalling. *Nat Cell Biol*. 15:1370-1377.

Edelstein, A.D., M.A. Tsuchida, N. Amodaj, H. Pinkard, R.D. Vale, and N. Stuurman. 2014. Advanced methods of microscope control using muManager software. *J Biol Methods*. 1.

Essex, A., A. Dammermann, L. Lewellyn, K. Oegema, and A. Desai. 2009. Systematic analysis in Caenorhabditis elegans reveals that the spindle checkpoint is composed of two largely independent branches. *Mol Biol Cell*. 20:1252-1267.

bioRxiv preprint doi: https://doi.org/10.1101/389080; this version posted November 4, 2019. The copyright holder for this preprint (which was not certified by peer review) is the author/funder, who has granted bioRxiv a license to display the preprint in perpetuity. It is made available under aCC-BY 4.0 International license.

Eytan, E., K. Wang, S. Miniowitz-Shemtov, D. Sitry-Shevah, S. Kaisari, T.J. Yen, S.T. Liu, and A. Hershko. 2014. Disassembly of mitotic checkpoint complexes by the joint action of the AAA-ATPase TRIP13 and p31(comet). *Proc Natl Acad Sci U S A*. 111:12019-12024.

Fava, L.L., M. Kaulich, E.A. Nigg, and A. Santamaria. 2011. Probing the in vivo function of Mad1:C-Mad2 in the spindle assembly checkpoint. *EMBO J*. 30:3322-3336.

Galli, M., and D.O. Morgan. 2016. Cell Size Determines the Strength of the Spindle Assembly Checkpoint during Embryonic Development. *Dev Cell*. 36:344-352.

Gerhold, A.R., V. Poupart, J.C. Labbe, and P.S. Maddox. 2018. Spindle assembly checkpoint strength is linked to cell fate in the Caenorhabditis elegans embryo. *Mol Biol Cell*. 29:1435-1448.

Gerhold, A.R., J. Ryan, J.N. Vallee-Trudeau, J.F. Dorn, J.C. Labbe, and P.S. Maddox. 2015. Investigating the regulation of stem and progenitor cell mitotic progression by in situ imaging. *Curr Biol*. 25:1123-1134.

Gotta, M., Y. Dong, Y.K. Peterson, S.M. Lanier, and J. Ahringer. 2003. Asymmetrically distributed C. elegans homologs of AGS3/PINS control spindle position in the early embryo. *Curr Biol*. 13:1029-1037.

Guo, S., and K.J. Kemphues. 1995. par-1, a gene required for establishing polarity in C. elegans embryos, encodes a putative Ser/Thr kinase that is asymmetrically distributed. *Cell*. 81:611-620.

Kyogoku, H., and T.S. Kitajima. 2017. Large Cytoplasm Is Linked to the Error-Prone Nature of Oocytes. *Dev Cell*. 41:287-298 e284.

Lawrence, K.S., T. Chau, and J. Engebrecht. 2015. DNA damage response and spindle assembly checkpoint function throughout the cell cycle to ensure genomic integrity. *PLoS Genet*. 11:e1005150.

bioRxiv preprint doi: https://doi.org/10.1101/389080; this version posted November 4, 2019. The copyright holder for this preprint (which was not certified by peer review) is the author/funder, who has granted bioRxiv a license to display the preprint in perpetuity. It is made available under aCC-BY 4.0 International license.

Li, Y., and R. Benezra. 1996. Identification of a human mitotic checkpoint gene: hsMAD2. *Science*. 274:246-248.

Luo, X., Z. Tang, J. Rizo, and H. Yu. 2002. The Mad2 spindle checkpoint protein undergoes similar major conformational changes upon binding to either Mad1 or Cdc20. *Mol Cell*. 9:59-71.

Luo, X., Z. Tang, G. Xia, K. Wassmann, T. Matsumoto, J. Rizo, and H. Yu. 2004. The Mad2 spindle checkpoint protein has two distinct natively folded states. *Nat Struct Mol Biol*. 11:338-345.

Ma, H.T., and R.Y. Poon. 2016. TRIP13 Regulates Both the Activation and Inactivation of the Spindle-Assembly Checkpoint. *Cell Rep*. 14:1086-1099.

Ma, H.T., and R.Y.C. Poon. 2018. TRIP13 Functions in the Establishment of the Spindle Assembly Checkpoint by Replenishing O-MAD2. *Cell Rep*. 22:1439-1450.

Maddox, A.S., B. Habermann, A. Desai, and K. Oegema. 2005. Distinct roles for two C. elegans anillins in the gonad and early embryo. *Development*. 132:2837-2848.

Mariani, L., E. Chiroli, L. Nezi, H. Muller, S. Piatti, A. Musacchio, and A. Ciliberto. 2012. Role of the Mad2 dimerization interface in the spindle assembly checkpoint independent of kinetochores. *Curr Biol*. 22:1900-1908.

Marks, D.H., R. Thomas, Y. Chin, R. Shah, C. Khoo, and R. Benezra. 2017. Mad2 Overexpression Uncovers a Critical Role for TRIP13 in Mitotic Exit. *Cell Rep*. 19:1832-1845.

Meraldi, P., V.M. Draviam, and P.K. Sorger. 2004. Timing and checkpoints in the regulation of mitotic progression. *Dev Cell*. 7:45-60.

Miniowitz-Shemtov, S., E. Eytan, S. Kaisari, D. Sitry-Shevah, and A. Hershko. 2015. Mode of interaction of TRIP13 AAA-ATPase with the Mad2-binding protein p31comet and with mitotic checkpoint complexes. *Proc Natl Acad Sci U S A*. 112:11536-11540.

bioRxiv preprint doi: https://doi.org/10.1101/389080; this version posted November 4, 2019. The copyright holder for this preprint (which was not certified by peer review) is the author/funder, who has granted bioRxiv a license to display the preprint in perpetuity. It is made available under aCC-BY 4.0 International license.

Moyle, M.W., T. Kim, N. Hattersley, J. Espeut, D.K. Cheerambathur, K. Oegema, and A. Desai. 2014. A Bub1-Mad1 interaction targets the Mad1-Mad2 complex to unattached kinetochores to initiate the spindle checkpoint. *J Cell Biol*. 204:647-657.

Nelson, C.R., T. Hwang, P.H. Chen, and N. Bhalla. 2015. TRIP13PCH-2 promotes Mad2 localization to unattached kinetochores in the spindle checkpoint response. *J Cell Biol*. 211:503-516.

Nezi, L., G. Rancati, A. De Antoni, S. Pasqualato, S. Piatti, and A. Musacchio. 2006. Accumulation of Mad2-Cdc20 complex during spindle checkpoint activation requires binding of open and closed conformers of Mad2 in Saccharomyces cerevisiae. *J Cell Biol*. 174:39-51.

Nystul, T.G., J.P. Goldmark, P.A. Padilla, and M.B. Roth. 2003. Suspended animation in C. elegans requires the spindle checkpoint. *Science*. 302:1038-1041.

O'Connell, K.F., C. Caron, K.R. Kopish, D.D. Hurd, K.J. Kemphues, Y. Li, and J.G. White. 2001. The C. elegans zyg-1 gene encodes a regulator of centrosome duplication with distinct maternal and paternal roles in the embryo. *Cell*. 105:547-558.

O'Rourke, S.M., C. Carter, L. Carter, S.N. Christensen, M.P. Jones, B. Nash, M.H. Price, D.W. Turnbull, A.R. Garner, D.R. Hamill, V.R. Osterberg, R. Lyczak, E.E. Madison, M.H. Nguyen, N.A. Sandberg, N. Sedghi, J.H. Willis, J. Yochem, E.A. Johnson, and B. Bowerman. 2011. A survey of new temperature-sensitive, embryonic-lethal mutations in C. elegans: 24 alleles of thirteen genes. *PLoS One*. 6:e16644.

Rodriguez-Bravo, V., J. Maciejowski, J. Corona, H.K. Buch, P. Collin, M.T. Kanemaki, J.V. Shah, and P.V. Jallepalli. 2014. Nuclear pores protect genome integrity by

bioRxiv preprint doi: https://doi.org/10.1101/389080; this version posted November 4, 2019. The copyright holder for this preprint (which was not certified by peer review) is the author/funder, who has granted bioRxiv a license to display the preprint in perpetuity. It is made available under aCC-BY 4.0 International license.

assembling a premitotic and Mad1-dependent anaphase inhibitor. *Cell*. 156:1017-1031.

Rose, L., and P. Gonczy. 2014. Polarity establishment, asymmetric division and segregation of fate determinants in early C. elegans embryos. *WormBook*:1-43.

Rosenberg, S.C., and K.D. Corbett. 2015. The multifaceted roles of the HORMA domain in cellular signaling. *J Cell Biol*. 211:745-755.

San-Segundo, P.A., and G.S. Roeder. 1999. Pch2 links chromatin silencing to meiotic checkpoint control. *Cell*. 97:313-324.

Seydoux, G., C.C. Mello, J. Pettitt, W.B. Wood, J.R. Priess, and A. Fire. 1996. Repression of gene expression in the embryonic germ lineage of C. elegans. *Nature*. 382:713-716.

Simonetta, M., R. Manzoni, R. Mosca, M. Mapelli, L. Massimiliano, M. Vink, B. Novak, A. Musacchio, and A. Ciliberto. 2009. The influence of catalysis on mad2 activation dynamics. *PLoS Biol*. 7:e10.

Sironi, L., M. Mapelli, S. Knapp, A. De Antoni, K.T. Jeang, and A. Musacchio. 2002. Crystal structure of the tetrameric Mad1-Mad2 core complex: implications of a 'safety belt' binding mechanism for the spindle checkpoint. *EMBO J*. 21:2496-2506.

Sironi, L., M. Melixetian, M. Faretta, E. Prosperini, K. Helin, and A. Musacchio. 2001. Mad2 binding to Mad1 and Cdc20, rather than oligomerization, is required for the spindle checkpoint. *EMBO J*. 20:6371-6382.

Srinivasan, D.G., R.M. Fisk, H. Xu, and S. van den Heuvel. 2003. A complex of LIN-5 and GPR proteins regulates G protein signaling and spindle function in C elegans. *Genes Dev*. 17:1225-1239.

bioRxiv preprint doi: https://doi.org/10.1101/389080; this version posted November 4, 2019. The copyright holder for this preprint (which was not certified by peer review) is the author/funder, who has granted bioRxiv a license to display the preprint in perpetuity. It is made available under aCC-BY 4.0 International license.

Sudakin, V., G.K. Chan, and T.J. Yen. 2001. Checkpoint inhibition of the APC/C in HeLa cells is mediated by a complex of BUBR1, BUB3, CDC20, and MAD2. *J Cell Biol*. 154:925-936.

Tintori, S.C., E. Osborne Nishimura, P. Golden, J.D. Lieb, and B. Goldstein. 2016. A Transcriptional Lineage of the Early C. elegans Embryo. *Dev Cell*. 38:430-444.

Tipton, A.R., K. Wang, P. Oladimeji, S. Sufi, Z. Gu, and S.T. Liu. 2012. Identification of novel mitosis regulators through data mining with human centromere/kinetochore proteins as group queries. *BMC Cell Biol*. 13:15.

Vader, G. 2015. Pch2(TRIP13): controlling cell division through regulation of HORMA domains. *Chromosoma*. 124:333-339.

van Hooff, J.J., E. Tromer, L.M. van Wijk, B. Snel, and G.J. Kops. 2017. Evolutionary dynamics of the kinetochore network in eukaryotes as revealed by comparative genomics. *EMBO Rep*.

Vazquez-Diez, C., L.M.G. Paim, and G. FitzHarris. 2019. Cell-Size-Independent Spindle Checkpoint Failure Underlies Chromosome Segregation Error in Mouse Embryos. *Curr Biol*. 29:865-873 e863.

Vleugel, M., E. Hoogendoorn, B. Snel, and G.J. Kops. 2012. Evolution and function of the mitotic checkpoint. *Dev Cell*. 23:239-250.

Wang, K., B. Sturt-Gillespie, J.C. Hittle, D. Macdonald, G.K. Chan, T.J. Yen, and S.T. Liu. 2014. Thyroid hormone receptor interacting protein 13 (TRIP13) AAA-ATPase is a novel mitotic checkpoint-silencing protein. *J Biol Chem*. 289:23928-23937.

Wu, H.Y., and S.M. Burgess. 2006. Two distinct surveillance mechanisms monitor meiotic chromosome metabolism in budding yeast. *Curr Biol*. 16:2473-2479.

bioRxiv preprint doi: https://doi.org/10.1101/389080; this version posted November 4, 2019. The copyright holder for this preprint (which was not certified by peer review) is the author/funder, who has granted bioRxiv a license to display the preprint in perpetuity. It is made available under aCC-BY 4.0 International license.

Ye, Q., S.C. Rosenberg, A. Moeller, J.A. Speir, T.Y. Su, and K.D. Corbett. 2015. TRIP13 is a protein-remodeling AAA+ ATPase that catalyzes MAD2 conformation switching. *eLife*. 4.

Yost, S., B. de Wolf, S. Hanks, A. Zachariou, C. Marcozzi, M. Clarke, R.M. de Voer, B. Etemad, E. Uijttewaal, E. Ramsay, H. Wylie, A. Elliott, S. Picton, A. Smith, S. Smithson, S. Seal, E. Ruark, G. Houge, J. Pines, G. Kops, and N. Rahman. 2017. Biallelic TRIP13 mutations predispose to Wilms tumor and chromosome missegregation. *Nat Genet*.

bioRxiv preprint doi: https://doi.org/10.1101/389080; this version posted November 4, 2019. The copyright holder for this preprint (which was not certified by peer review) is the author/funder, who has granted bioRxiv a license to display the preprint in perpetuity. It is made available under aCC-BY 4.0 International license.

Figure Legends

Figure 1: PCH-2 becomes dispensable for the spindle checkpoint response in somatic cells experimentally reduced in size

(A) Images of control and *ani-2*^{RNAi} two-cell embryos. Scale bar indicates 5 µm. (B) Cartoon of embryos treated with *zyg-1*^{RNAi} or *ani-2*^{RNAi}*;zyg-1*^{RNAi}. (C) Mitotic timing, as measured from nuclear envelope breakdown (NEBD) to the onset of cortical contractility (OCC), in AB cells of control, *pch-2* and *mad-1* mutant embryos plotted against cell volume. Lines represent regression analysis for each set of data. (D) Data from (C) partitioned into three categories: wild-type sized embryos (more than 5 x 10^3 µm^3), medium sized embryos (between 3.5 x 10^3 µm^3 and 5 x 10^3 µm^3) and small embryos (less than 3.5 x 10^3 µm^3). Error bars are S.E.M. In all graphs, a * indicates a p value < 0.05, ** indicates a p value < 0.01 and *** a p value < 0.0001.

Figure 2: PCH-2 becomes dispensable for MAD-2 recruitment at unattached kinetochores in somatic cells experimentally reduced in size

(A) Cartoon and images of GFP::MAD-2 recruitment to unattached kinetochores in AB cells of small and wild-type sized embryos. Scale bar indicates 1 µm. (B) Quantification of kinetochore bound GFP::MAD-2. Error bars are S.E.M.

Figure 3: MAD-2 dosage controls checkpoint strength

(A) Immunostaining of MAD-2 and nuclear pore complex components (NPCs) shows MAD-2 localized in the nucleus and at the nuclear envelope during interphase. Scale bar indicates 5 µm. (B) Model depicting how a decrease cell volume might result in an increase in the local concentration of O-Mad2 in *ani-2*^{RNAi}*;zyg-1*^{RNAi} embryos, in contrast to *zyg-1*^{RNAi} embryos. (C) Mitotic timing, as measured from nuclear envelope breakdown

bioRxiv preprint doi: https://doi.org/10.1101/389080; this version posted November 4, 2019. The copyright holder for this preprint (which was not certified by peer review) is the author/funder, who has granted bioRxiv a license to display the preprint in perpetuity. It is made available under aCC-BY 4.0 International license.

(NEBD) to the onset of cortical contractility (OCC), in AB cells of control and *mad-2/+* mutant embryos plotted against cell volume. Lines represent regression analysis for each set of data.

Figure 4: PCH-2 is required for the spindle checkpoint response during embryogenesis

(A) Mitotic timing, as measured from nuclear envelope breakdown (NEBD) to decondensation of chromatin (DECON), in control, *pch-2* and *san-1* mutant embryos treated with nocodazole at different developmental stages (4- and 16-cell embryos). (B) Mitotic timing in control and *pch-2* mutant embryos overexpressing GFP::MAD-2 and treated with nocodazole at different developmental stages (4- and 16-cell embryos). (C) Mitotic timing in *zyg-1*^{ts} and *pch-2;zyg-1*^{ts} mutant embryos at different developmental stages (2-, 4- and 8-cell embryos). All error bars are S.E.M.

Figure 5: PCH-2 is responsible for the stronger spindle checkpoint in the germline lineage

Mitotic timing, as measured from nuclear envelope breakdown (NEBD) to the onset of cortical contractility (OCC), in AB and P_1 cells plotted against cell volume in control *ani-2*^{RNAi}*;zyg-1*^{RNAi} embryos (A) or *pch-2;ani-2*^{RNAi}*;zyg-1*^{RNAi} (B) embryos. Lines represent regression analysis for each set of data. Data for AB cells in both control and *pch-2* mutants is the same as in Figure 1C. (C) Mitotic timing of AB and P_1 cells in control, *pch-2* and *mad-1* mutants during unperturbed divisions. Error bars are S.E.M.

Figure 6: PCH-2's enrichment in P_1 cells depends on PAR-1

(A) Mitotic timing of control embryos and embryos expressing PCH-2::GFP during unperturbed divisions or in the presence of monopolar spindles. (B) Cartoon and images

bioRxiv preprint doi: https://doi.org/10.1101/389080; this version posted November 4, 2019. The copyright holder for this preprint (which was not certified by peer review) is the author/funder, who has granted bioRxiv a license to display the preprint in perpetuity. It is made available under aCC-BY 4.0 International license.

of PCH-2::GFP localization around mitotic chromosomes in AB and P_1 cells of two-cell embryos. Scale bar indicates 5 µm. (C) Quantification of PCH-2::GFP fluorescence in AB and P_1 cells. (D) Cartoon and images of PCH-2::GFP localization around mitotic chromosomes in AB and P_1 cells of control RNAi and *par-1*^{RNAi} two-cell embryos. (E) Quantification of PCH-2::GFP fluorescence in AB and P_1 cells of *par-1*^{RNAi} embryos. All error bars are S.E.M. NS indicates not significant.

Figure 7: The stronger checkpoint in P_1 cells depends on CMT-1

(A) Mitotic timing, as measured from nuclear envelope breakdown (NEBD) to the onset of cortical contractility (OCC), in AB and P_1 cells plotted against cell volume in *cmt-1;ani-2*^{RNAi}*;zyg-1*^{RNAi} embryos. Lines represent regression analysis for each set of data. (B) Mitotic timing of control, *cmt-1* and *mad-1* mutant embryos during unperturbed divisions or in the presence of monopolar spindles. (C) Cartoon and images of PCH-2::GFP localization around mitotic chromosomes in AB and P_1 cells of *cmt-1* mutant embryos. Scale bar indicates 5 µm. (D) Quantification of PCH-2::GFP fluorescence in AB cells of control and *cmt-1* mutant embryos. (E) Quantification of PCH-2::GFP fluorescence in AB and P_1 cells of *cmt-1* mutant embryos. All error bars are S.E.M. NS indicates not significant.

Figure 8: Model

(A) A robust spindle checkpoint response in large cells requires the presence of PCH-2 at unattached kinetochores to increase the local concentration O-MAD-2 at and near unattached kinetochores. (B) Reducing cell volume of two-cell embryos increases the concentration of O-Mad-2 at and near unattached kinetochores, allowing a checkpoint response in the absence of PCH-2. (C) The enrichment of PCH-2 around mitotic

bioRxiv preprint doi: https://doi.org/10.1101/389080; this version posted November 4, 2019. The copyright holder for this preprint (which was not certified by peer review) is the author/funder, who has granted bioRxiv a license to display the preprint in perpetuity. It is made available under aCC-BY 4.0 International license.

chromosomes in P_1 cells results in a higher production of O-MAD-2, generating a stronger spindle checkpoint response in these cells.

Figure S1: Related to Figure 1. The mitotic delay observed in *pch-2;ani-2^{RNAi};zyg-1^{RNAi}* small cells is a spindle checkpoint response.

Cartoon of control and *ani-2^{RNAi}* two-cell embryos (A) and an *ani-2^{RNAi};zyg-1^{RNAi}* two-cell embryo (B). Mitotic timing in AB cells plotted against cell volume, during unperturbed mitosis (C) and in the presence of monopolar spindles. (D). Lines represent regression analysis for each set of data. The regression line of *pch-2;ani-2^{RNAi};zyg-1^{RNAi}* embryos from Figure 1C is indicated by the opaque red line for comparison.

Figure S2: Related to Figure 2: GFP::MAD-2 decreases at unattached kinetochores in the AB cells of small *ani-2^{RNAi};zyg-1^{RNAi}* embryos, unlike in *pch-2;ani-2^{RNAi};zyg-1^{RNAi}* embryos.

(A) Quantification of GFP::MAD-2 fluorescence at unattached kinetochores plotted against cell volume in AB cells of control and *pch-2* embryos. Lines represent regression analysis for each set of data. (B) Quantification of GFP::MAD-2 fluorescence around mitotic chromosomes in AB cells of control and *pch-2* embryos plotted against cell volume. (C) Images of MAD-2::GFP in AB cells of control *ani-2^{RNAi};zyg-1^{RNAi}* embryos or *pch-2;ani-2^{RNAi};zyg-1^{RNAi}* embryos. Scale bar indicates 5 µm.

Figure S3: Related to Figure 3. Nuclear volume does not scale with cell volume in *ani-2^{RNAi}* two-cell embryos.

(A) Images of a large (top) and small (bottom) AB cell of *ani-2^{RNAi}* embryos. The nuclear area is indicated with a dashed yellow line. Scale bar indicates 5 µm. (B) Nuclear area plotted against cell volume.

bioRxiv preprint doi: https://doi.org/10.1101/389080; this version posted November 4, 2019. The copyright holder for this preprint (which was not certified by peer review) is the author/funder, who has granted bioRxiv a license to display the preprint in perpetuity. It is made available under aCC-BY 4.0 International license.

Figure S4: Related to Figure 5. PCH-2 is responsible for the stronger spindle checkpoint in the germline lineage.

(A) Mitotic timing of control and *pch-2* mutant embryos during unperturbed divisions or in the presence of monopolar spindles. Data for control embryos is the same as Figure 7B. (B) Mitotic timing, as measured from nuclear envelope breakdown (NEBD) to the onset of cortical contractility (OCC), in AB and P_1 cells plotted against cell volume in control *ani-2*^{RNAi}*;zyg-1*^{RNAi} embryos or *pch-2;ani-2*^{RNAi}*;zyg-1*^{RNAi} embryos. Lines represent regression analysis for each set of data.

Figure S5: Related to Figure 6. There is no difference in the amount of PCH-2::GFP or GFP::MAD-2 recruited to unattached kinetochores in AB and P_1 cells.

(A) Cartoon and images of PCH-2::GFP recruitment to unattached kinetochores in AB and P_1 cells of two-cell embryos. Scale bar indicates 1 µm. (B) Quantification of PCH-2::GFP recruitment at unattached kinetochores in AB and P_1 cells. (C) Cartoon and images of GFP::MAD-2 recruitment to unattached kinetochores in AB and P_1 cells of two-cell embryos. Scale bar indicates 1 µm. (D) Quantification of GFP::MAD-2 fluorescence at unattached kinetochores in AB and P_1 cells. All error bars are S.E.M. NS indicates not significant.

Figure S6: Related to Figure 6. There is no difference in the amount of PCH-2::GFP in the cytoplasm of AB and P_1 cells.

(A) Images of AB (left) and P_1 (right) cells after NEBD. Scale bar indicate 5 µm. (B) Quantification of PCH-2::GFP fluorescence in the cytoplasm of AB and P_1 cells. Error bars are S.E.M. NS indicates not significant.

bioRxiv preprint doi: https://doi.org/10.1101/389080; this version posted November 4, 2019. The copyright holder for this preprint (which was not certified by peer review) is the author/funder, who has granted bioRxiv a license to display the preprint in perpetuity. It is made available under aCC-BY 4.0 International license.

Figure S7: Related to Figure 6. PCH-2's enrichment in P_1 cells depends on GPR-1/2. (A) Images of two cell embryos treated with control RNAi or RNAi against *gpr-1* and *gpr-2*. (B) Cartoon and images of PCH-2::GFP localization around mitotic chromosomes in AB and P_1 cells of control RNAi and *gpr-1/2*^{RNAi} two-cell embryos. Scale bars indicate 5 µm. (C) Quantification of PCH-2::GFP fluorescence in AB and P_1 cells of *gpr-1/2*^{RNAi} embryos. Error bars are S.E.M.

Movie legends

Video 1

Mitosis in the AB cell of a wild-type sized control two-cell embryo with monopolar spindles expressing GFH::PH and mCherry::H2B for visualization of the plasma membrane and the chromosomes, respectively (strain OD95). The timer starts at NEBD.

Video 2

Mitosis in the AB cell of a small control two-cell embryo with monopolar spindles expressing GFH::PH and mCherry::H2B for visualization of the plasma membrane and the chromosomes, respectively (strain OD95). The timer starts at NEBD.

Video 3

Mitosis in the AB cell of a wild-type sized *pch-2(tm1458)* two-cell embryo with monopolar spindles expressing GFH::PH and mCherry::H2B for visualization of the plasma membrane and the chromosomes, respectively (strain BHL575). The timer starts at NEBD.

Video 4

bioRxiv preprint doi: https://doi.org/10.1101/389080; this version posted November 4, 2019. The copyright holder for this preprint (which was not certified by peer review) is the author/funder, who has granted bioRxiv a license to display the preprint in perpetuity. It is made available under aCC-BY 4.0 International license.

Mitosis in the AB cell of a small *pch-2(tm1458)* two-cell embryo with monopolar spindles expressing GFH::PH and mCherry::H2B for visualization of the plasma membrane and the chromosomes, respectively (strain BHL575). The timer starts at NEBD.

Video 5

Mitosis in the P_1 cell of a wild-type sized control two-cell embryo with monopolar spindles expressing GFH::PH and mCherry::H2B for visualization of the plasma membrane and the chromosomes, respectively (strain OD95). The timer starts at NEBD.

Video 6

Mitosis in the P_1 cell of a small control two-cell embryo with monopolar spindles expressing GFH::PH and mCherry::H2B for visualization of the plasma membrane and the chromosomes, respectively (strain OD95). The timer starts at NEBD.

Video 7

Mitosis in the P_1 cell of a wild-type sized *pch-2(tm1458)* two-cell embryo with monopolar spindles expressing GFH::PH and mCherry::H2B for visualization of the plasma membrane and the chromosomes, respectively (strain BHL575). The timer starts at NEBD.

Video 8

Mitosis in the P_1 cell of a small *pch-2(tm1458)* two-cell embryo with monopolar spindles expressing GFH::PH and mCherry::H2B for visualization of the plasma membrane and the chromosomes, respectively (strain BHL575). The timer starts at NEBD.

Video 9

bioRxiv preprint doi: https://doi.org/10.1101/389080; this version posted November 4, 2019. The copyright holder for this preprint (which was not certified by peer review) is the author/funder, who has granted bioRxiv a license to display the preprint in perpetuity. It is made available under aCC-BY 4.0 International license.

Mitosis in the AB cell of a wild-type sized *cmt-1(ok2879)* two-cell embryo with monopolar spindles expressing GFH::PH and mCherry::H2B for visualization of the plasma membrane and the chromosomes, respectively (strain BHL608). The timer starts at NEBD.

Video 10

Mitosis in the AB cell of a small *cmt-1(ok2879)* two-cell embryo with monopolar spindles expressing GFH::PH and mCherry::H2B for visualization of the plasma membrane and the chromosomes, respectively (strain BHL608). The timer starts at NEBD.

Video 11

Mitosis in the P_1 cell of a wild-type sized *cmt-1(ok2879)* two-cell embryo with monopolar spindles expressing GFH::PH and mCherry::H2B for visualization of the plasma membrane and the chromosomes, respectively (strain BHL608). The timer starts at NEBD.

Video 12

Mitosis in the P_1 cell of a small *cmt-1(ok2879)* two-cell embryo with monopolar spindles expressing GFH::PH and mCherry::H2B for visualization of the plasma membrane and the chromosomes, respectively (strain BHL608). The timer starts at NEBD.

bioRxiv preprint doi: https://doi.org/10.1101/389080; this version posted November 4, 2019. The copyright holder for this preprint (which was not certified by peer review) is the author/funder, who has granted bioRxiv a license to display the preprint in perpetuity. It is made available under aCC-BY 4.0 International license.

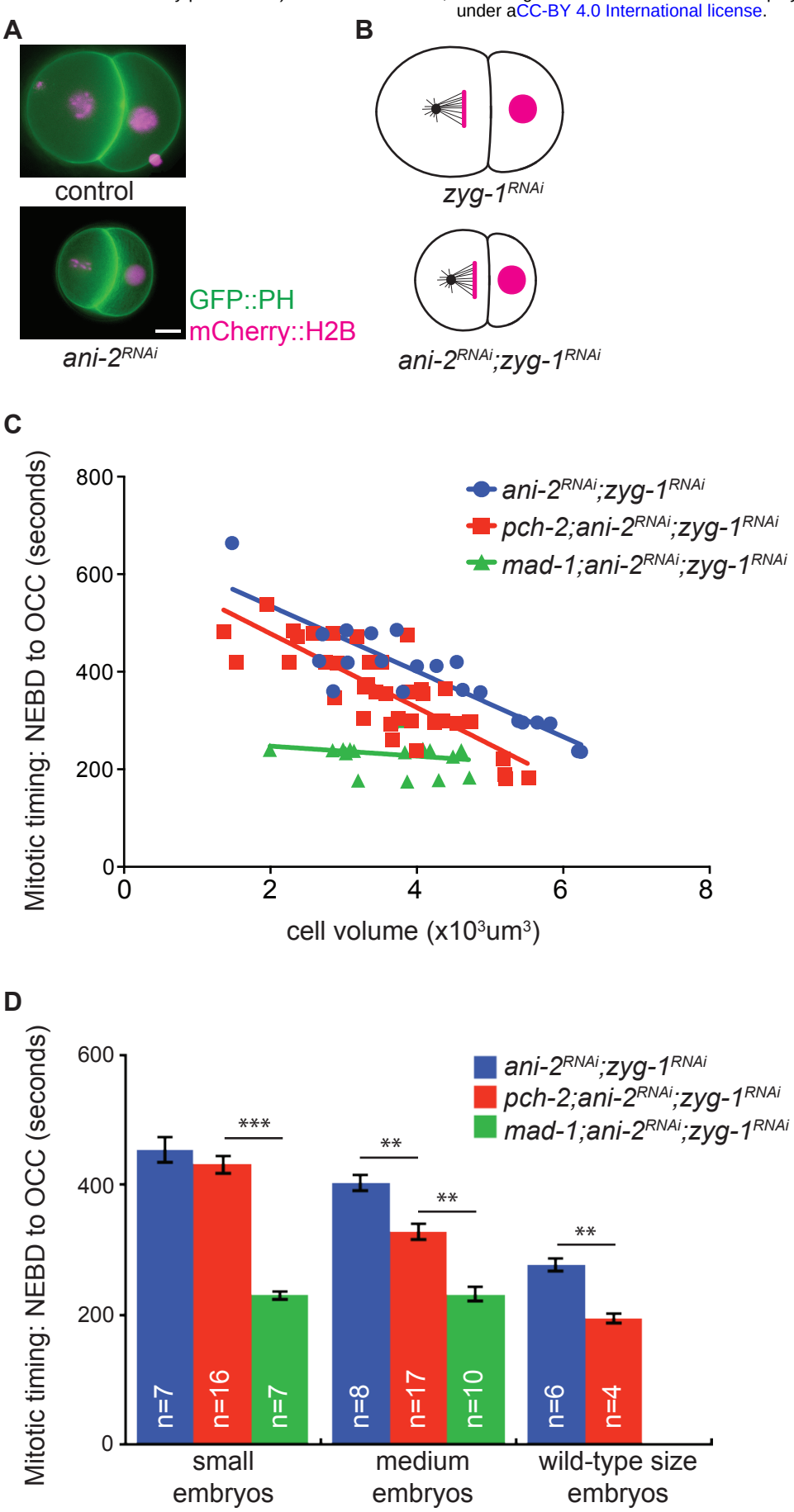

bioRxiv preprint doi: https://doi.org/10.1101/389080; this version posted November 4, 2019. The copyright holder for this preprint (which was not certified by peer review) is the author/funder, who has granted bioRxiv a license to display the preprint in perpetuity. It is made available under aCC-BY 4.0 International license.

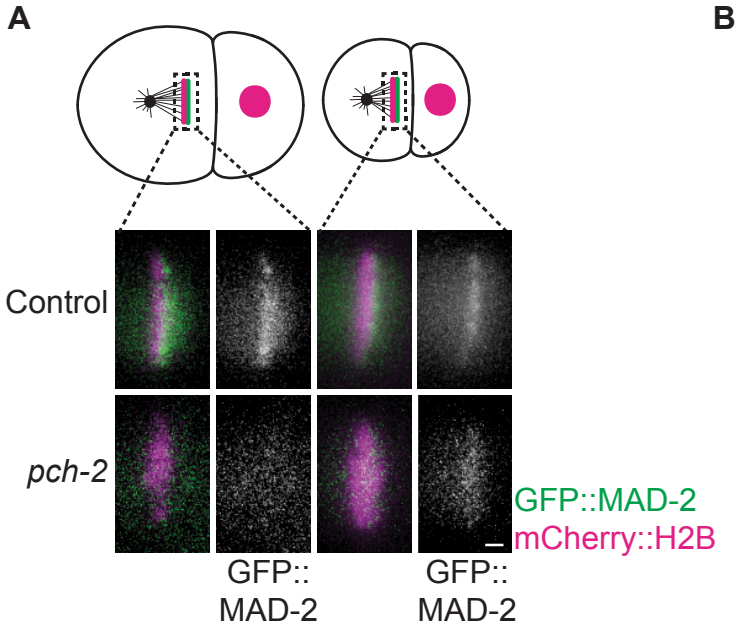

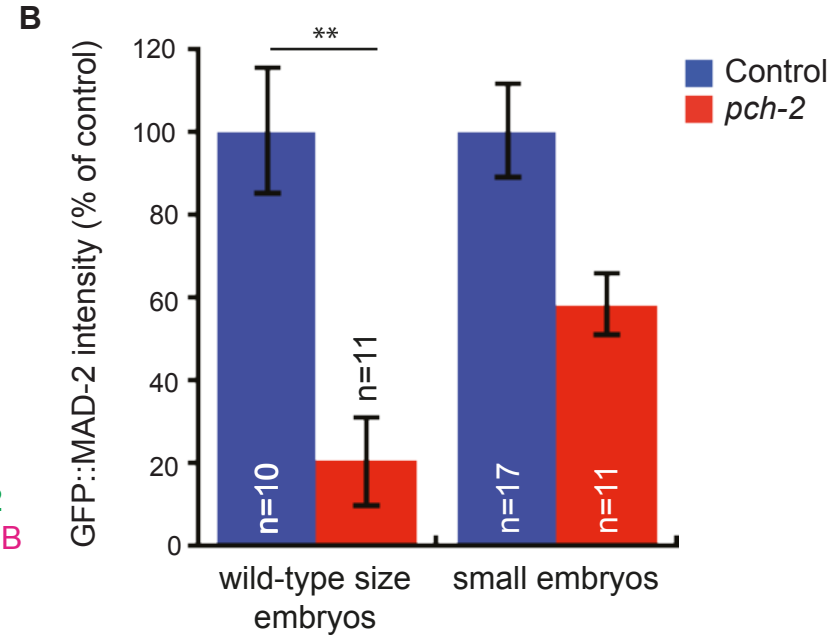

bioRxiv preprint doi: https://doi.org/10.1101/389080; this version posted November 4, 2019. The copyright holder for this preprint (which was not certified by peer review) is the author/funder, who has granted bioRxiv a license to display the preprint in perpetuity. It is made available under aCC-BY 4.0 International license.

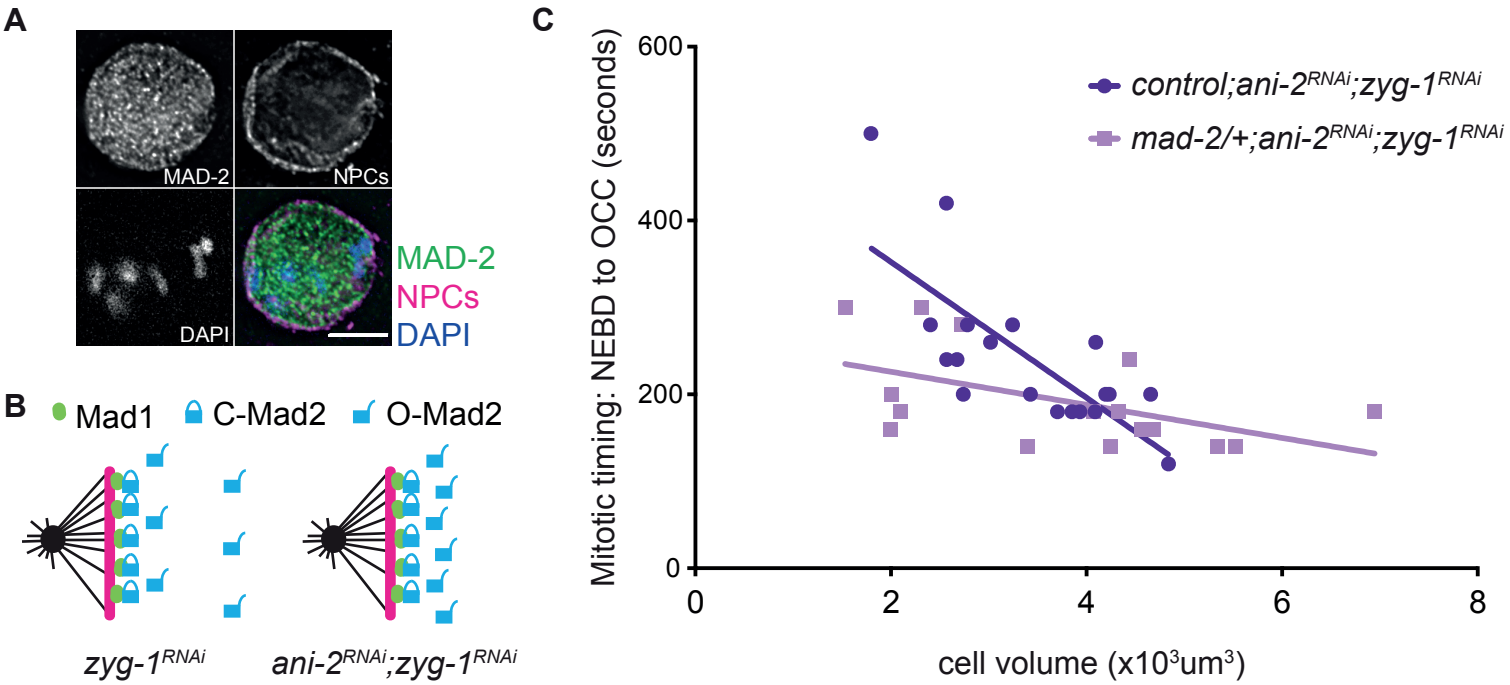

bioRxiv preprint doi: https://doi.org/10.1101/389080; this version posted November 4, 2019. The copyright holder for this preprint (which was not certified by peer review) is the author/funder, who has granted bioRxiv a license to display the preprint in perpetuity. It is made available under aCC-BY 4.0 International license.

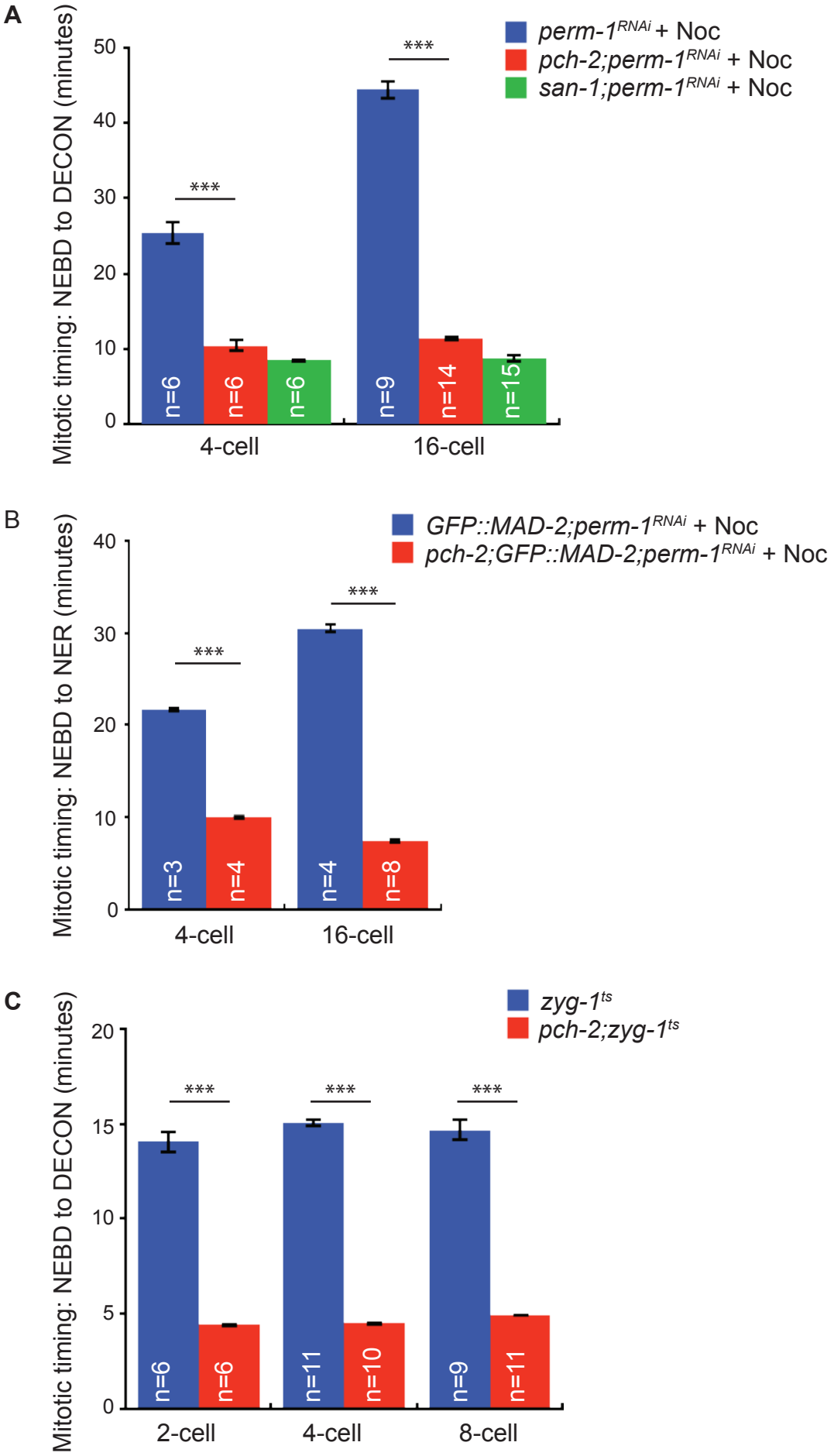

bioRxiv preprint doi: https://doi.org/10.1101/389080; this version posted November 4, 2019. The copyright holder for this preprint (which was not certified by peer review) is the author/funder, who has granted bioRxiv a license to display the preprint in perpetuity. It is made available under aCC-BY 4.0 International license.

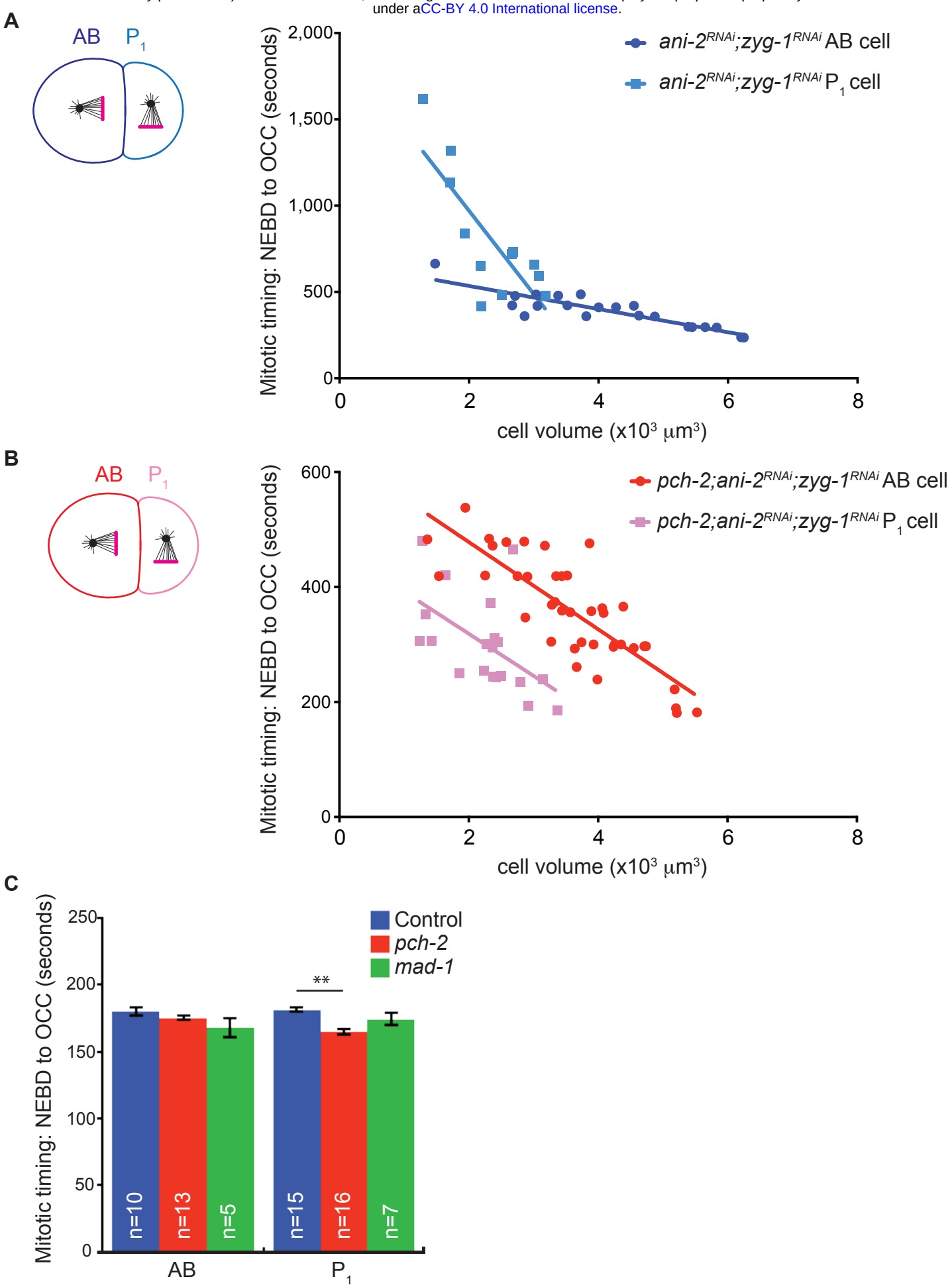

bioRxiv preprint doi: https://doi.org/10.1101/389080; this version posted November 4, 2019. The copyright holder for this preprint (which was not certified by peer review) is the author/funder, who has granted bioRxiv a license to display the preprint in perpetuity. It is made available under aCC-BY 4.0 International license.

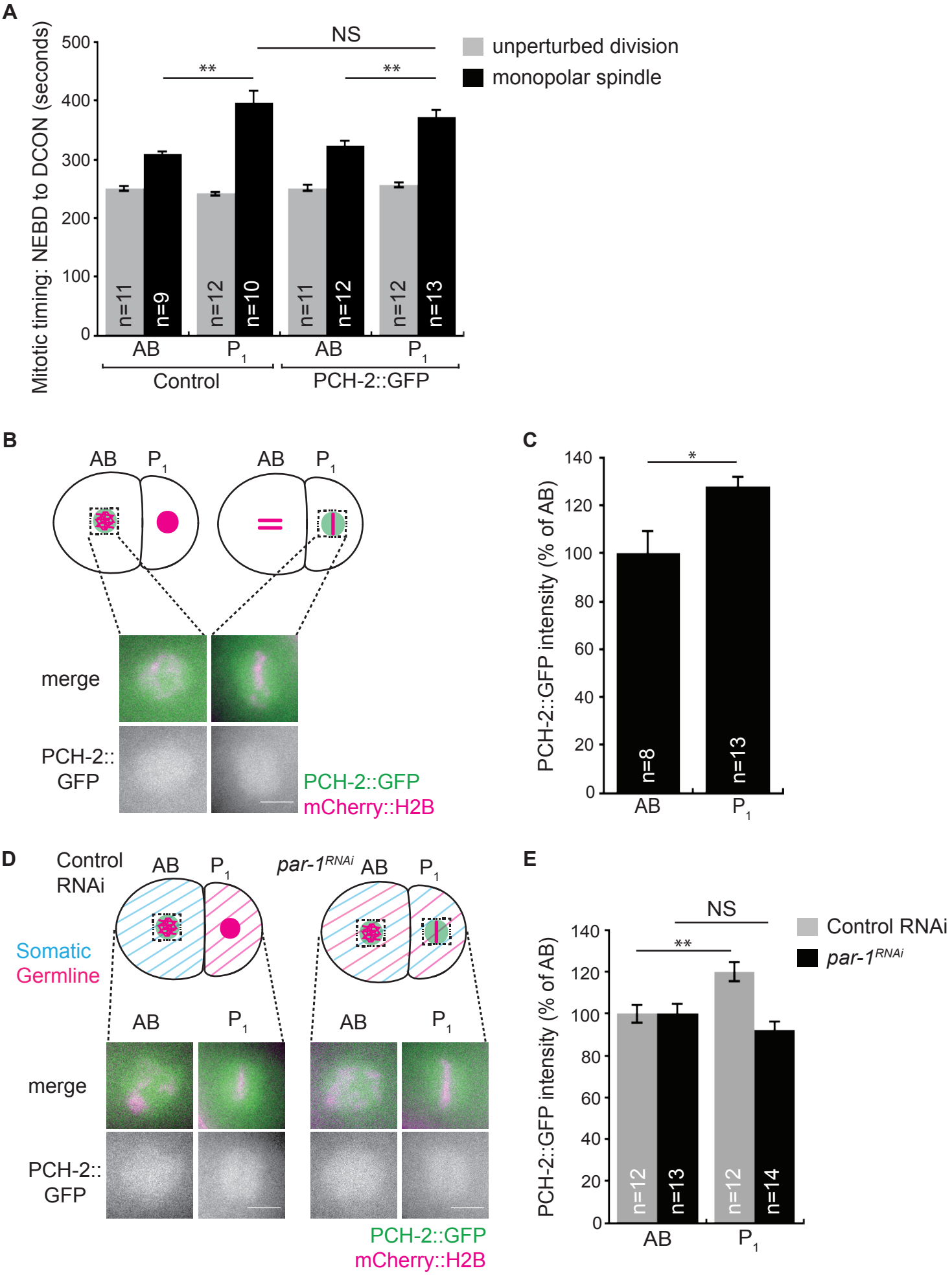

bioRxiv preprint doi: https://doi.org/10.1101/389080; this version posted November 4, 2019. The copyright holder for this preprint (which was not certified by peer review) is the author/funder, who has granted bioRxiv a license to display the preprint in perpetuity. It is made available under aCC-BY 4.0 International license.

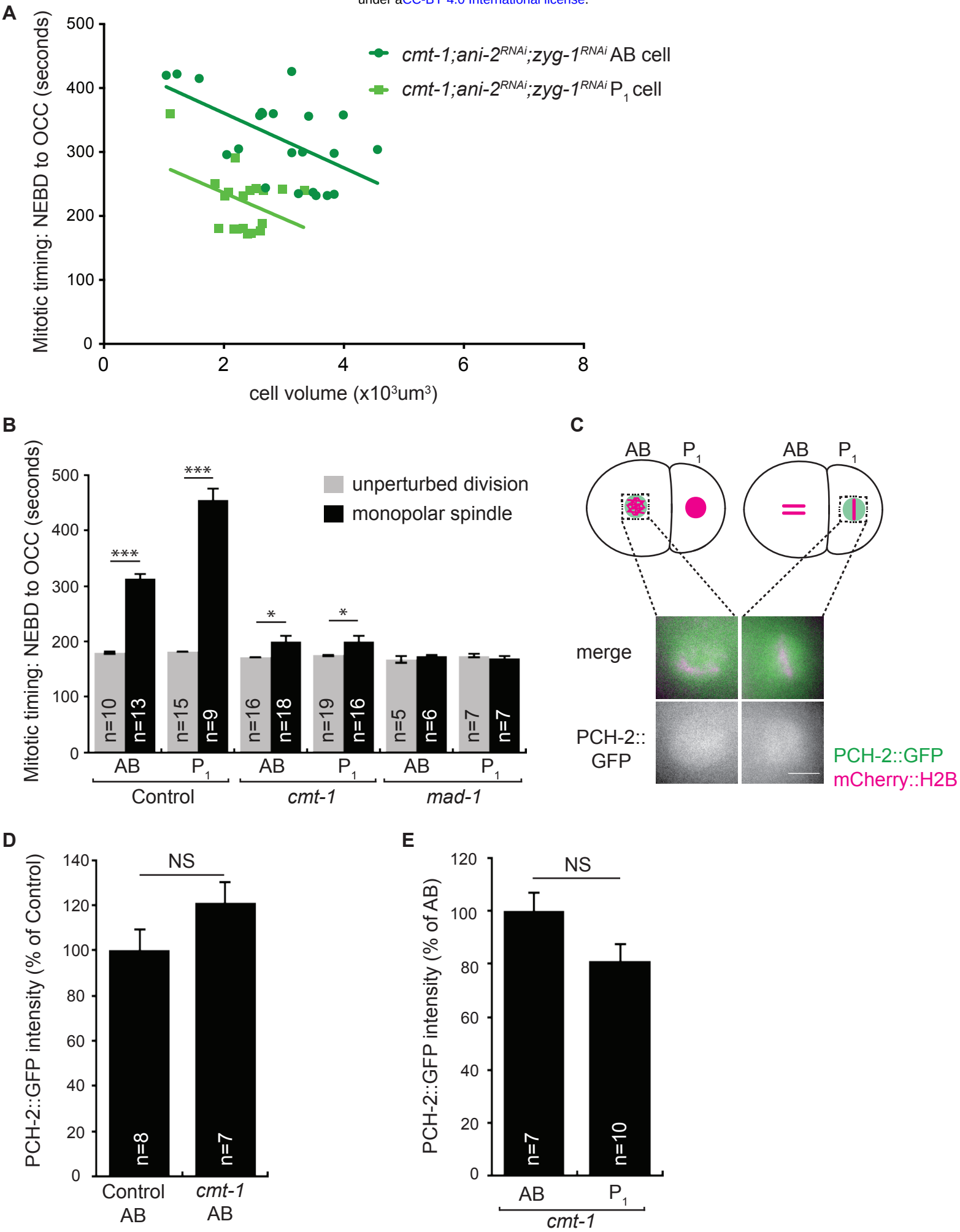

bioRxiv preprint doi: https://doi.org/10.1101/389080; this version posted November 4, 2019. The copyright holder for this preprint (which was not certified by peer review) is the author/funder, who has granted bioRxiv a license to display the preprint in perpetuity. It is made available under aCC-BY 4.0 International license.

Détachelles et al. Figure 8

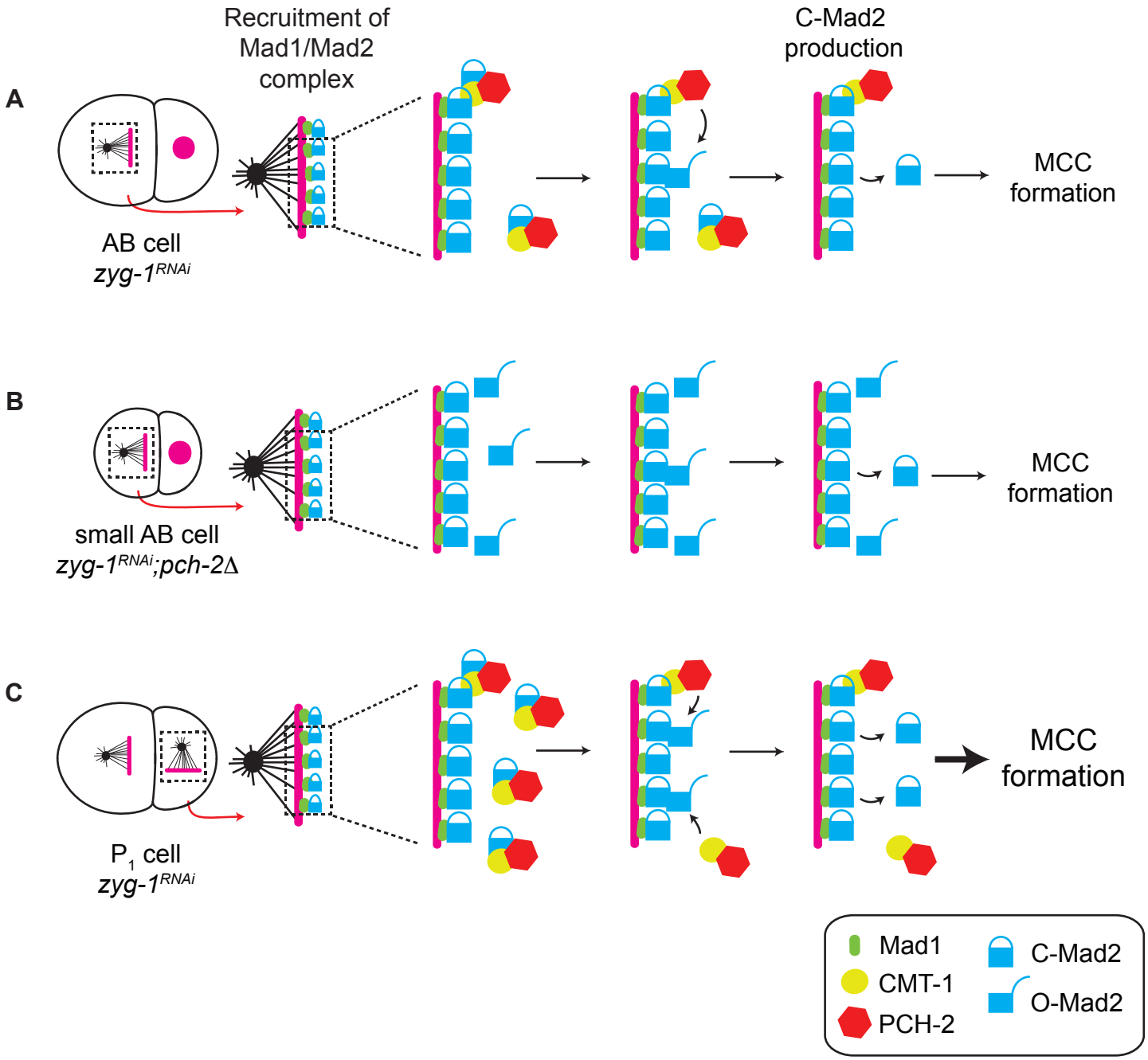

bioRxiv preprint doi: https://doi.org/10.1101/389080; this version posted November 4, 2019. The copyright holder for this preprint (which was not certified by peer review) is the author/funder, who has granted bioRxiv a license to display the preprint in perpetuity. It is made available under aCC-BY 4.0 International license.

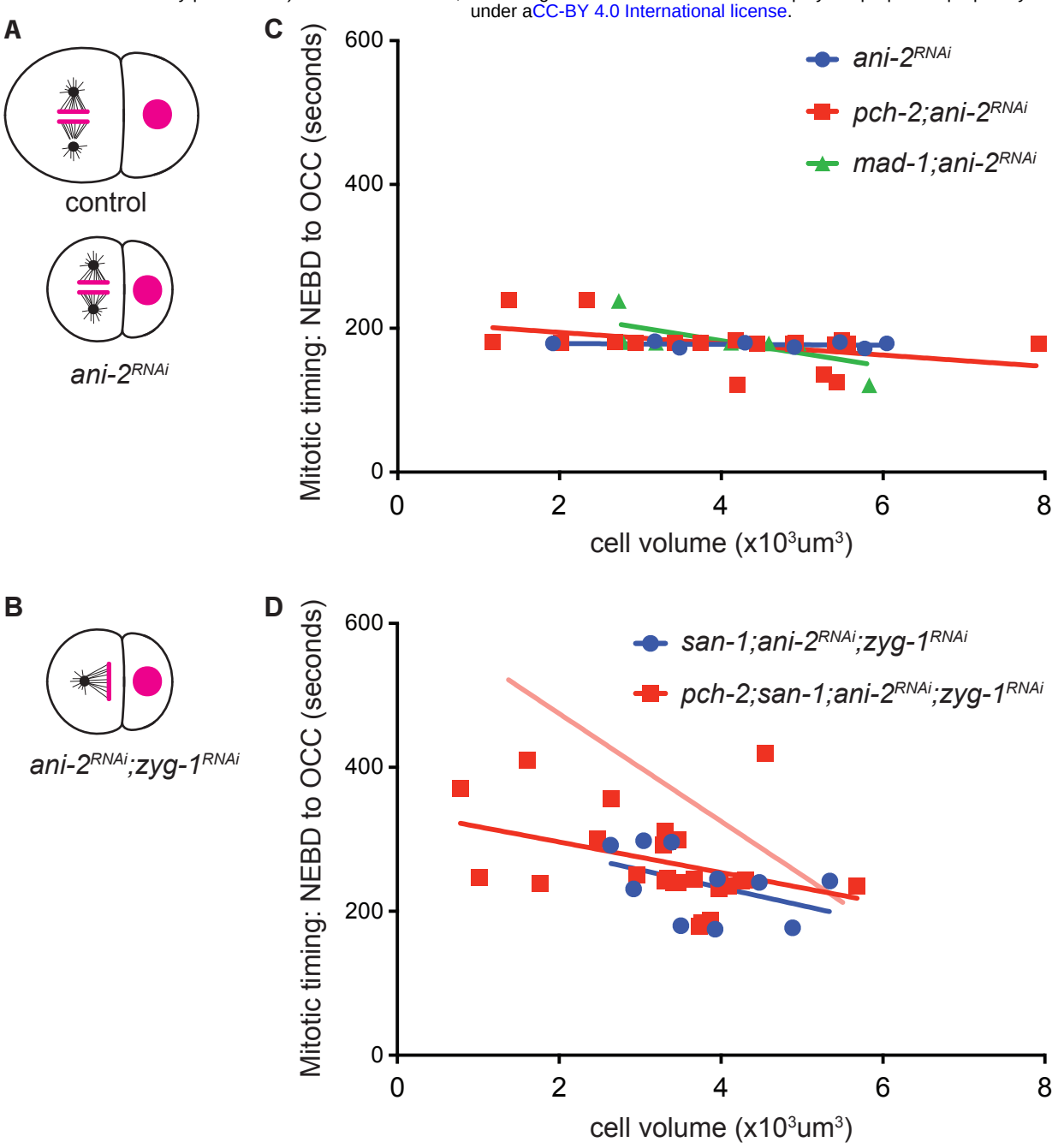

bioRxiv preprint doi: https://doi.org/10.1101/389080; this version posted November 4, 2019. The copyright holder for this preprint (which was not certified by peer review) is the author/funder, who has granted bioRxiv a license to display the preprint in perpetuity. It is made available under aCC-BY 4.0 International license.

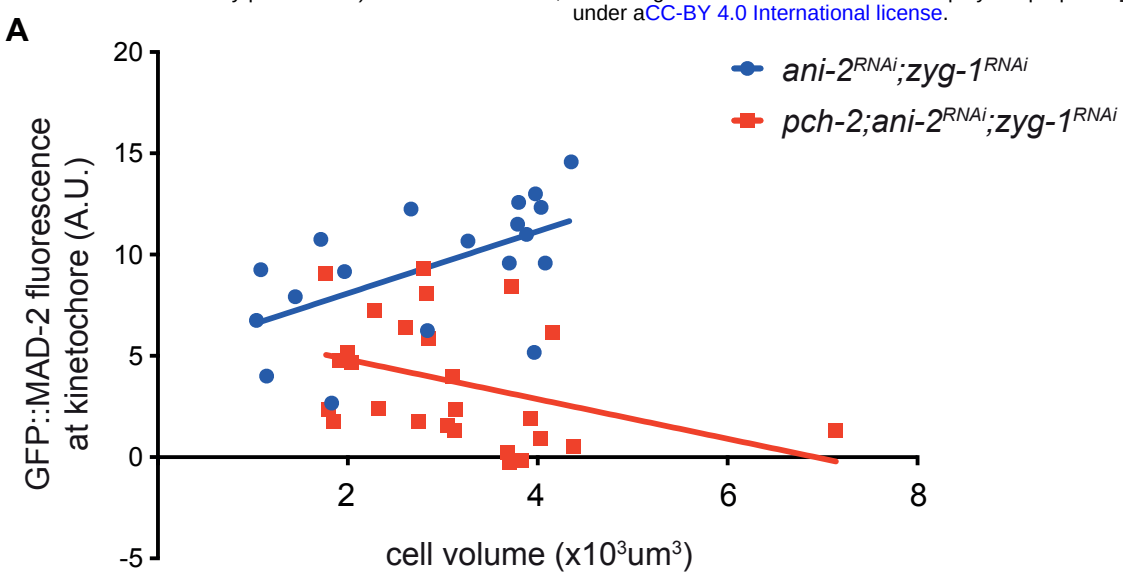

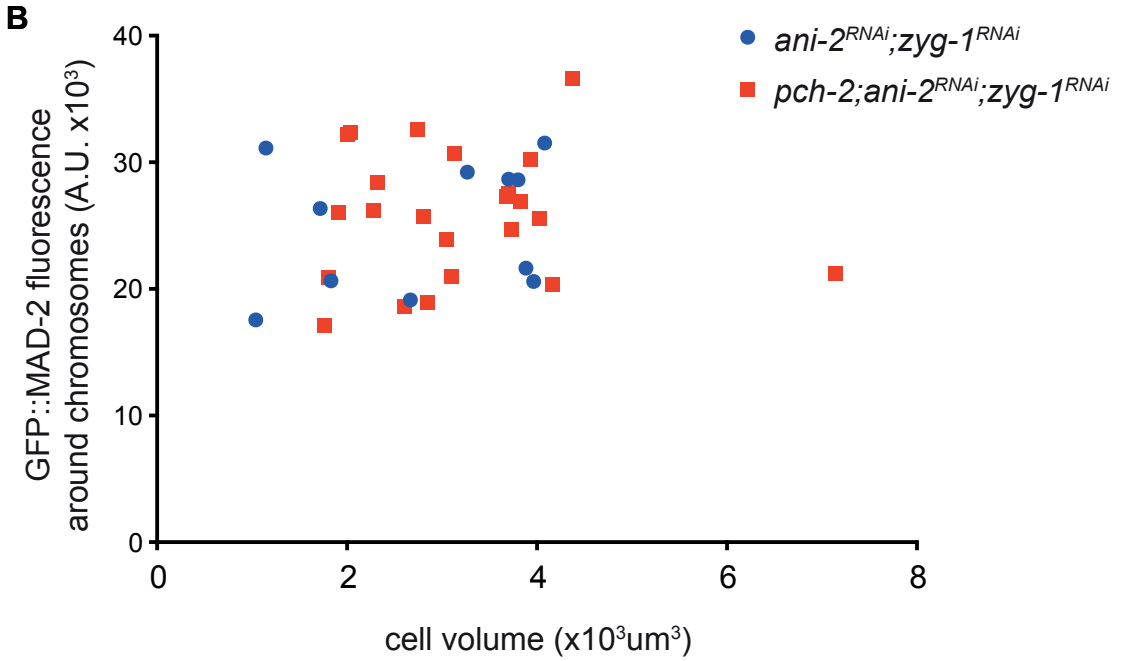

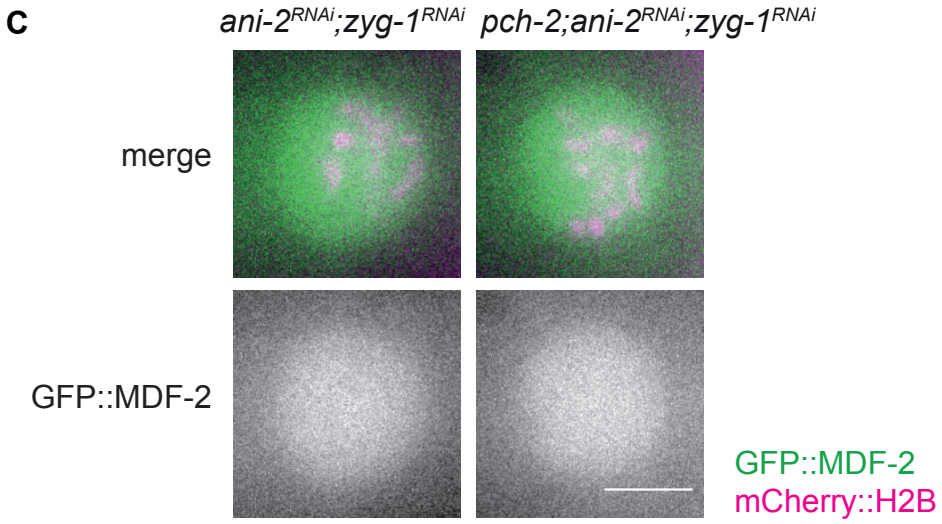

bioRxiv preprint doi: https://doi.org/10.1101/389080; this version posted November 4, 2019. The copyright holder for this preprint (which was not certified by peer review) is the author/funder, who has granted bioRxiv a license to display the preprint in perpetuity. It is made available under aCC-BY 4.0 International license.

Defachelles et al. Figure S3

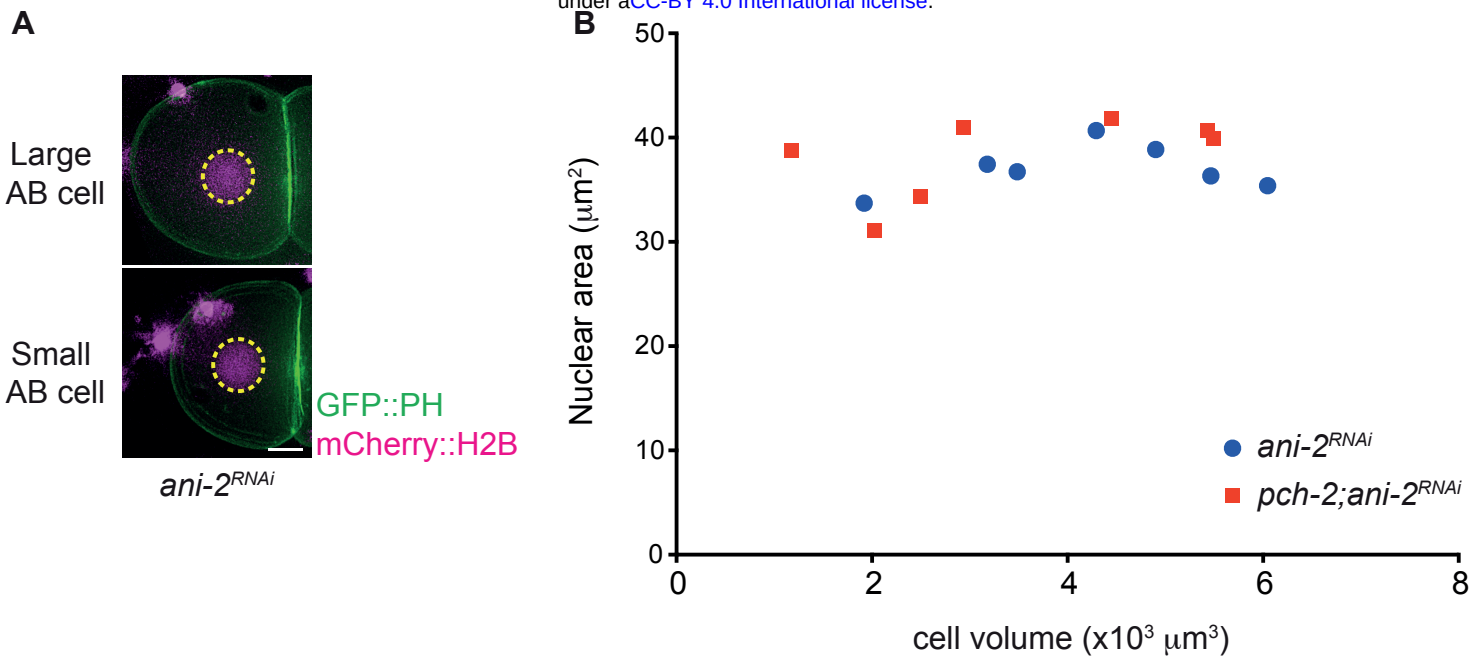

bioRxiv preprint doi: https://doi.org/10.1101/389080; this version posted November 4, 2019. The copyright holder for this preprint (which was not certified by peer review) is the author/funder, who has granted bioRxiv a license to display the preprint in perpetuity. It is made available under aCC-BY 4.0 International license.

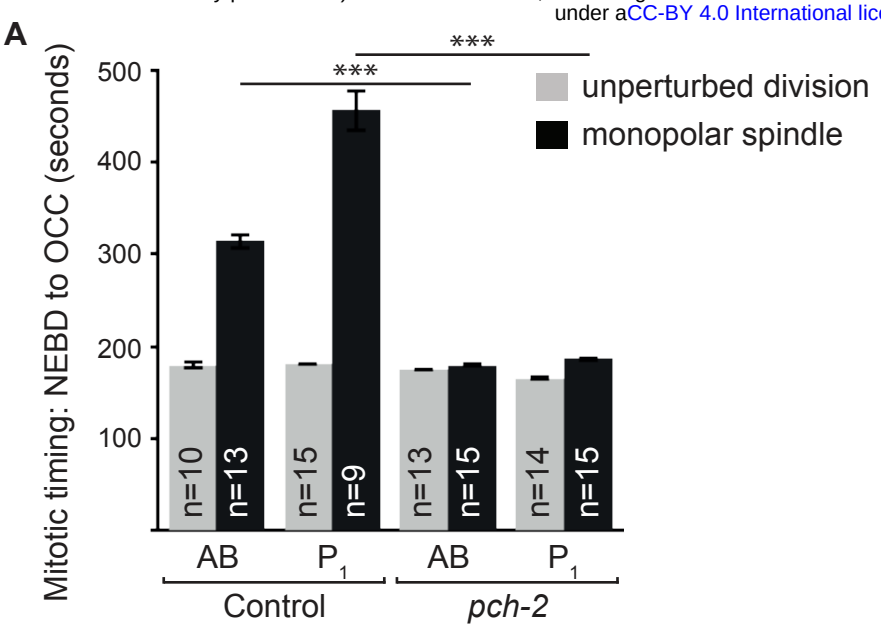

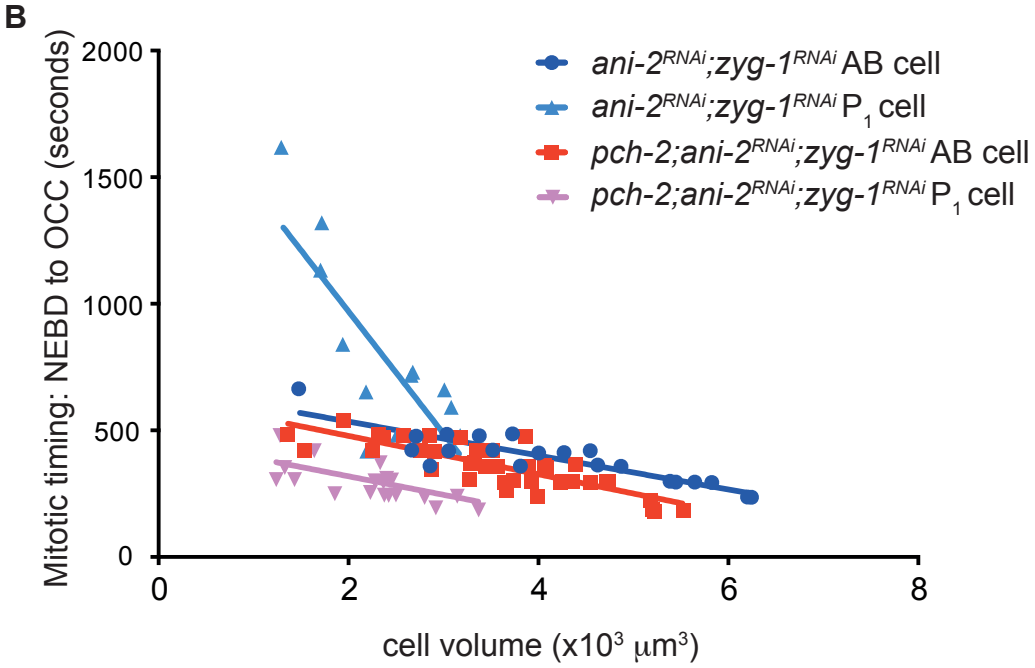

bioRxiv preprint doi: https://doi.org/10.1101/389080; this version posted November 4, 2019. The copyright holder for this preprint (which was not certified by peer review) is the author/funder, who has granted bioRxiv a license to display the preprint in perpetuity. It is made available under aCC-BY 4.0 International license.

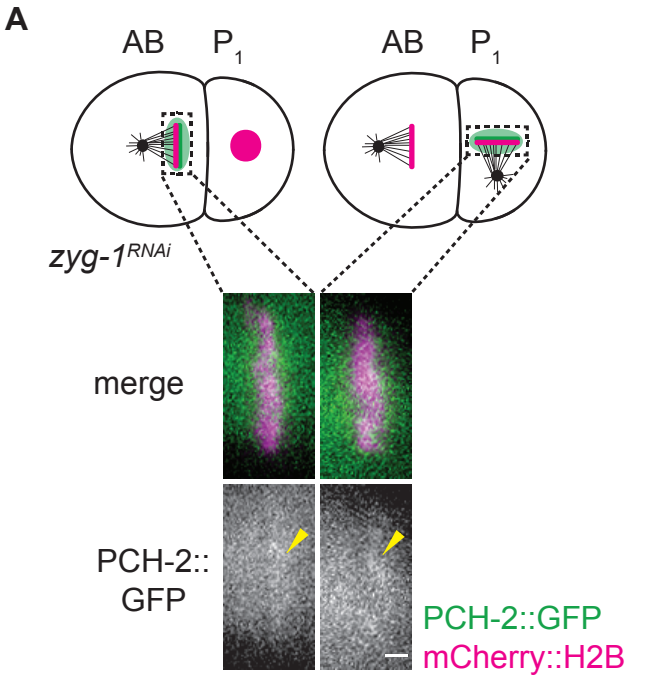

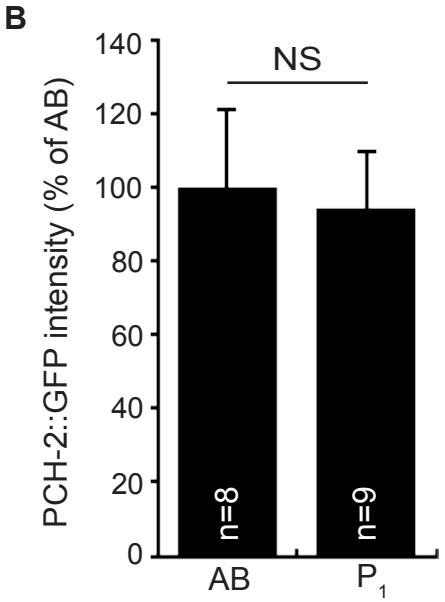

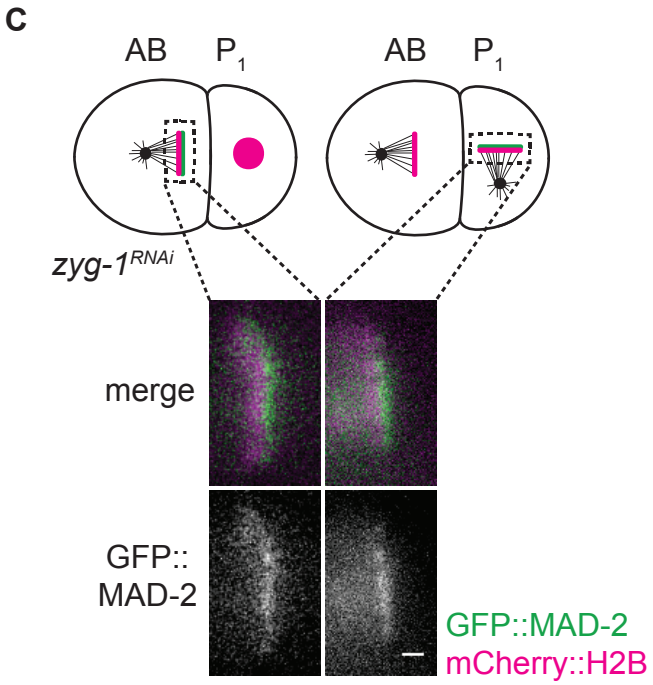

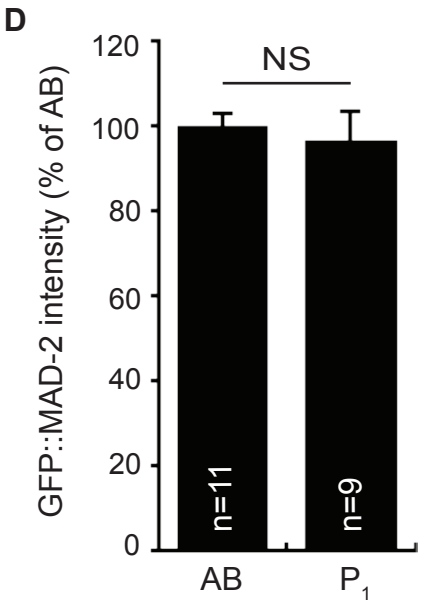

bioRxiv preprint doi: https://doi.org/10.1101/389080; this version posted November 4, 2019. The copyright holder for this preprint (which was not certified by peer review) is the author/funder, who has granted bioRxiv a license to display the preprint in perpetuity. It is made available under aCC-BY 4.0 International license.

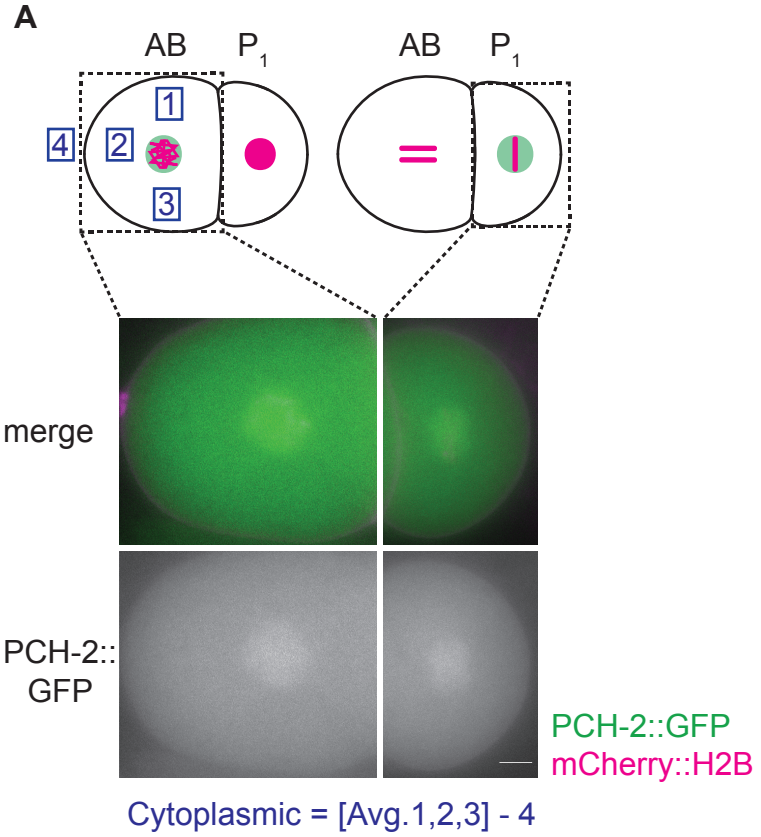

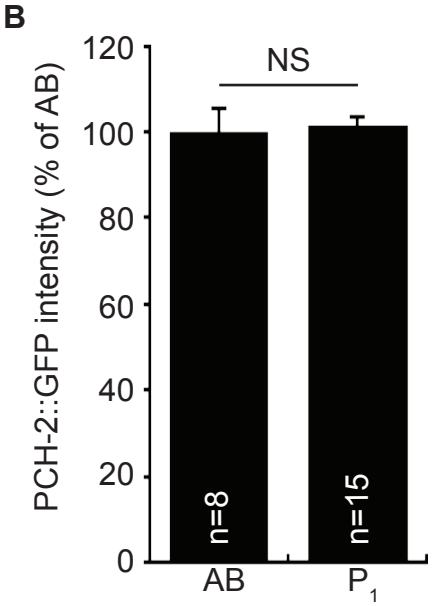

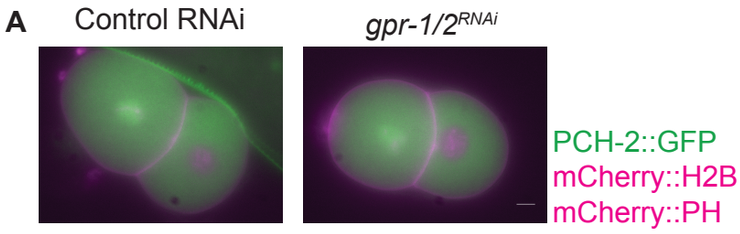

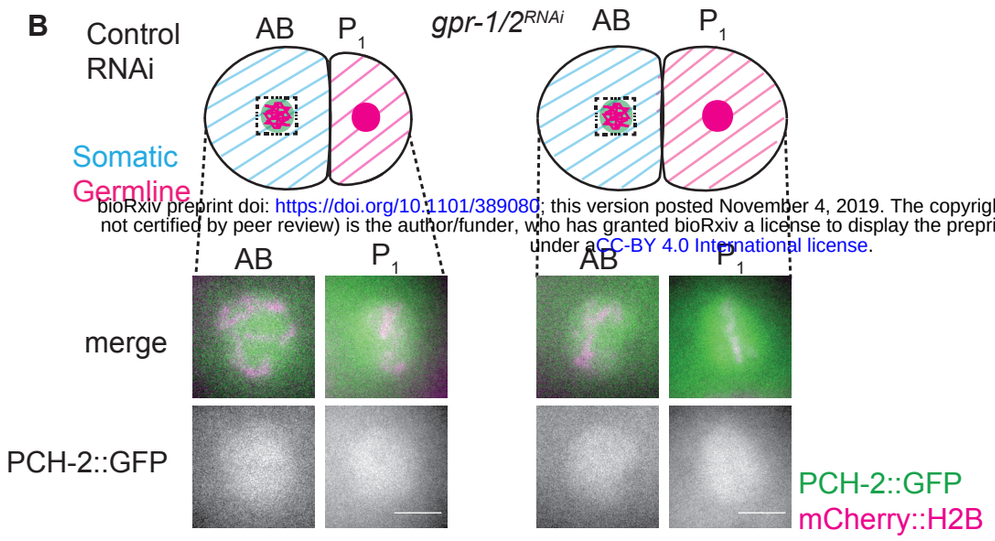

bioRxiv preprint doi: https://doi.org/10.1101/389080; this version posted November 4, 2019. The copyright holder for this preprint (which was not certified by peer review) is the author/funder, who has granted bioRxiv a license to display the preprint in perpetuity. It is made available under aCC-BY 4.0 International license.

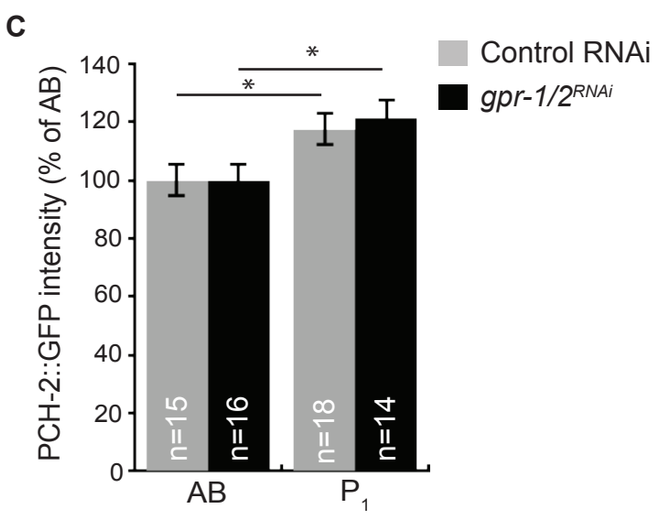

bioRxiv preprint doi: https://doi.org/10.1101/389080; this version posted November 4, 2019. The copyright holder for this preprint (which was not certified by peer review) is the author/funder, who has granted bioRxiv a license to display the preprint in perpetuity. It is made available under aCC-BY 4.0 International license.

Table S1: Strains used in this study

Strain	Genotype
OD56	*unc-119(ed3) III; ltIs37 [pAA64; Ppie-1::mCherry::his-58; unc-119 (+)] IV*
OD95	*unc-119(ed3) III; ltIs37 [pAA64; Ppie-1::mCherry::his-58; unc-119 (+)] IV; ltIs38 [pAA1; Ppie-1::GFP::PH(PLC1delta1); unc-119(+)]*
BHL575	*pch-2(tm1458) II; unc-119(ed3) III; ltIs37 [pAA64; Ppie-1::mCherry::his-58; unc-119 (+)] IV; ltIs38 [pAA1;Ppie-1::GFP::PH(PLC1delta1); unc-119(+)]*
BHL596	*unc-119(ed3) III; ltIs37 [pAA64; Ppie-1::mCherry::his-58; unc-119 (+)] IV; ltIs38 [pAA1; Ppie-1::GFP::PH(PLC1delta1); unc-119(+)]; mdf-1(av19) V*
BHL600	*unc-119(ed3) III; ltIs37 [pAA64; Ppie-1::mCherry::his-58; unc-119 (+)] IV; ltIs52 [pOD379; Ppie-1::GFP::MDF-2; unc-119 (+)]*
BHL604	*pch-2(tm1458) II; unc-119(ed3) III; ltIs37 [pAA64; Ppie-1::mCherry::his-58; unc-119 (+)] IV; ltIs52 [pOD379; Ppie-1::GFP::MDF-2; unc-119 (+)]*
BHL608	*cmt-1(ok2879) I; unc-119(ed3) III; ltIs37 [pAA64; Ppie-1::mCherry::his-58; unc-119 (+)] IV; ltIs38 [pAA1;Ppie-1::GFP::PH(PLC1delta1); unc-119(+)]*
BHL664	*Ppch-2::pch-2::GFP-3XFLAG (blt4 [pCN94]) II; unc-119(ed3) III; ltIs37 [pAA64; Ppie-1::mCherry::his-58; unc-119 (+)] IV*
BHL666	*unc-119(ed3) III; ltIs37 [pAA64; Ppie-1::mCherry::his-58; unc-119 (+)];mdf-2(tm2190) IV/nT1[qIs51](IV;V) ltIs38 [pAA1; Ppie-1::GFP::PH(PLC1delta1); unc-119(+)]*
BHL883	*san-1/mdf-3 (ok1580) I; pch-2(tm1458) II; unc-119(ed3) III; ltIs37 [pAA64; Ppie-1::mCherry::his-58; unc-119 (+)] IV; ltIs38 [pAA1; Ppie-1::GFP::PH(PLC1delta1); unc-119(+)]*
BHL887	*cmt-1(ok2879) I; pch-2::GFP-3XFLAG (blt4 [pCN94]) II; unc-119(ed3) III; ltIs44[pAA173; pPie-1::mCherry::PH(PLC1delta1); unc-119(+)]; ltIs37 [pAA64; Ppie-1::mCherry::his-58; unc-119 (+)] IV*
BHL888	*unc-119(ed3) III; ltIs44 [pAA173; pPie-1::mCherry::PH(PLC1delta1); unc-119(+)]; ltIs52 [pOD379; Ppie-1::GFP::mdf-2; unc-119 (+)]; ltIs37 [pAA64; Ppie-1::mCherry::his-58; unc-119 (+)] IV*
BHL889	*pch-2(tm1458) II; unc-119(ed3) III; ltIs44 [pAA173; pPie-1::mCherry::PH(PLC1delta1); unc-119(+)]; ltIs52 [pOD379; Ppie-1::GFP::mdf-2; unc-119 (+)]; ltIs37 [pAA64; Ppie-1::mCherry::his-58; unc-119 (+)] IV*
BHL891	*unc-119(ed3) III; ltIs37 [pAA64; Ppie-1::mCherry::his-58; unc-119 (+)] IV; ltIs24[pAZ132; pPie-1::GFP::tba-2; unc-119(+)]*
BHL892	*pch-2 (tm1458) II; unc-119(ed3) III; ltIs37 [pAA64; Ppie-1::mCherry::his-58; unc-119 (+)] IV; ltIs24 [pAZ132; pPie-1::GFP::tba-2; unc-119(+)]*
BHL893	*san-1/mdf-3 (ok1580) I; unc-119(ed3) III; ltIs37 [pAA64; Ppie-1::mCherry::his-58; unc-119 (+)] IV; ltIs38 [pAA1; Ppie-1::GFP::PH(PLC1delta1); unc-119(+)]*
BHL904	*Ppch-2::pch-2::GFP-3XFLAG (blt4 [pCN94]) II; unc-119(ed3) III; ltIs44[pAA173; pPie-1::mCherry::PH(PLC1delta1); unc-119(+)]; ltIs37 [pAA64; Ppie-1::mCherry::his-58; unc-119 (+)] IV*
BHL950	*pch-2(tm1458) II; unc-119(ed3) III; ltIs37 [pAA64; Ppie-1::mCherry::his-58; unc-119 (+)]; mdf-2(tm2190) IV/nT1[qIs51](IV;V); ltIs38 [pAA1; Ppie-1::GFP::PH(PLC1delta1); unc-119(+)]*

bioRxiv preprint doi: https://doi.org/10.1101/389080; this version posted November 4, 2019. The copyright holder for this preprint (which was not certified by peer review) is the author/funder, who has granted bioRxiv a license to display the preprint in perpetuity. It is made available under aCC-BY 4.0 International license.

BHL958	*unc-119(ed3) III; ltIs37 [pAA64; Ppie-1::mCherry::his-58; unc-119 (+)] IV/nT1[qIs51](IV;V); ltIs38 [pAA1; Ppie-1::GFP::PH(PLC1delta1); unc-119(+)]*
BHL964	*zyg-1(or297) unc-4(e120) II unc-119(ed3) III; ltIs37 [pAA64; Ppie-1::mCherry::his-58; unc-119 (+)] IV; ltIs24[pAZ132; pPie-1::GFP::tba-2; unc-119(+)]*
BHL965	*zyg-1(or297) pch-2(tm1458) unc-4(e120) II; unc-119(ed3) III; ltIs37 [pAA64; Ppie-1::mCherry::his-58; unc-119 (+)] IV; ltIs24[pAZ132; pPie-1::GFP::tba-2; unc-119(+)]*
GAL5	*san-1/mdf-3 (mat5) I; unc-119(ed3) III; ruIs57[Ppie-1::GFP::tubulin + unc-119(+)]; ltIs37[pie-1p::mCherry::his-58 (pAA64) + unc-119(+)] IV*